The Pennsylvania State University

The Graduate School

College of Earth and Mineral Sciences

VAPOR GROWTH OF SMALL ICE CRYSTALS AT LOW TEMPERATURES IN AN ELECTRODYNAMIC LEVITATION DIFFUSION CHAMBER

A Thesis in

Meteorology

by

Alexander William Harrison

Submitted in Partial Fulfillment
of the Requirements
for the Degree of

Master of Science

December 2013

The thesis of Alexander William Harrison was reviewed and approved* by the following:

Jerry Y. Harrington
Associate Professor of Meteorology
Thesis Advisor

Johannes Verlinde
Professor of Meteorology
Associate Head, Graduate Program in Meteorology

Eugene E. Clothiaux
Professor of Meteorology

William H. Brune
Professor of Meteorology
Head of the Department of Meteorology

*Signatures are on file in the Graduate School

Abstract

An experimental Button Electrode Levitation (BEL) diffusion chamber for the growth of small (15 μm to 100 μm radius) ice crystals has been developed and used to produce new ice crystal growth measurements at temperatures near -30 °C. The use of a diffusion chamber allows for controlled growth in stable conditions for high and low supersaturations over ice ranging from 2% to 25%. The temperature inside the chamber can be determined with relatively high precision (to about 0.1 K); however, determination of the saturation state has greater error (typically around 20% reaching a maximum of 50%). Both the accuracy and the practical use of the device were greatly improved by developing software to automatically track, control, and record the growth of the particles. Mass growth data from the BEL chamber are used to test the traditional capacitance model and the Kinetically Limited Adaptive Habit (KLAH) model. The KLAH model is able to reproduce the shape and magnitude of the laboratory data within measured precision that the universally used capacitance is unable to replicate. The KLAH model was also used to determine the critical supersaturations and their dependence on temperature from -30 °C to -35 °C. Critical supersaturations derived from minimizing the error between the KLAH solutions and the laboratory data compare well with values derived from prior studies. Between -30 °C and -34 °C, the critical supersaturation is typically in the range of 3% to 5%; however, a substantial rise in the critical supersaturation occurs at -35 °C. KLAH predicts the axis-averaged deposition coefficients (α) based on the temperature and critical supersaturation, and these were determined to be below 0.1 for most cases, and as low as 0.004. These results are similar

to a number of prior laboratory studies, but are at odds with recent measurements taken in the AIDA chamber. Finally, results from the BEL diffusion chamber suggest that ice particle growth may depend on initial size, as has been postulated. Particles grown in the same BEL chamber environment tend to become more massive if their initial radius is below 9 μm.

Table of Contents

List of Figures

List of Tables

Acknowledgements

This work was funded through the National Science Foundation under Grant AGS-0951807.

I would like to express my gratitude to my advisor Jerry Harrington for the opportunity to work on such a grand project and for his continual support in completing this project. I have learned more than I could have ever thought possible about the field of ice physics and beyond.

Thank you to everyone who has had an important role in this project: Al Moyle for building the instrument and providing repairs when necessary as well as developing (with the help of Ray Shaw) an alternative to our greatest (glass) hardship, Chengzhu (Jill) Zhang for creating the model central to this project, my committee Johannes Verlinde and Eugene Clothiaux for providing valuable comments and insight, Ben Sherman for being a willing successor on this project, and Burkely Twiest for providing impromptu luck during the first successful particle growth.

Thanks to Azam Noon, Paul Bauch, and Stephen Nichols for providing a great place to live and great friends outside of the Walker Building. Many thanks go to my parents for housing, feeding, and supporting me during the composition of my thesis.

Finally, I cannot say enough to thank Kristen Koprowski for all the support and encouragement throughout the duration of my work at Penn State.

Chapter 1

Introduction and Motivation

Macroscopically, ice crystals represent, depending on one's viewpoint, a chilly inconvenience falling from the sky, or the building blocks of cirrus clouds and mixed-phase precipitation. The dendritic ice crystals familiar to the world are only a small portion of the ice crystal types found in nature. Each ice crystal begins its existence high in the atmosphere as water vapor. This vapor either deposits onto an ice nucleus or forms a supercooled water drop with a radius of several micrometers before freezing. The newly formed ice crystal's growth is highly dependent upon the thermal and saturation characteristics of the environment surrounding the particle. In situ measurements of ice growth within clouds would be invaluable. The remoteness of clouds, however, as well as the inability to obtain data beyond snapshots of ice crystals, prevents direct ice growth measurements in clouds. Laboratory instruments simulating the sub-freezing environments experienced by growing crystals in clouds are a common solution to studying individual ice crystal growth (e.g. Libbrecht, 2003).

The basic shape of individual ice crystals, excluding polycrystals, is generally a hexagonal prism with two basal faces capping six prism faces. Not all crystals possess regular hexagonal facets (i.e. one set of basal and prism faces); but a hexagonal prism provides a useful proxy for their underlying structure. Atmospheric ice at nearly every temperature has a crystallographic structure consistent with this hexagonal symmetry. For example, dendritic snowflakes are complex structures, but they can form from an initial

hexagonal particle. Dendrites can also often be characterized by a circumscribed hexagon. These crystals are commonly called "single" crystals and are characterized by a c-dimension equal to half the distance between basal faces and an a-dimension equal to the radius of a circle circumscribing the basal face. Together, these axes define the primary habit (or shape) of ice crystals and is usually quantified by the aspect ratio φ (φ = c/a); for plate-like particles, φ<1 and for column-like particles φ>1. Complexities in ice growth arise depending on the temperature, saturation, and even nucleation (Bailey and Hallett, 2004), causing variation of crystal habit. While temperature appears to define the primary habit of most crystals at temperatures above about -20 °C, saturation determines the secondary habits of ice crystals (Nakaya, 1954; Kobayashi, 1960; Bailey and Hallett, 2009). For instance, at temperatures between -12 °C and -16 °C, dendritic and stellar crystals form from the underlying hexagonal plate structure. At temperatures near -5 °C, needle crystals appear as well as hollowed columns (see Fig 1.1).

Crystals can take on multiple growth characteristics if they are transported to different growth environments. Plates may grow in one region of a cloud (say at -15 °C), but columns will grow from the regions of the hexagonal tips of the plates if they are advected into a temperature regime where columnar growth dominates (-4 °C to -9 °C). Similarly, columns may begin growth at one temperature (-5 °C for example), but advection to temperatures where plate growth is favored (-10 °C to -20 °C) can cause plate-topped "capped" columns to form. Clearly, it is important to understand the growth rates and paths of single crystals under a variety of environmental conditions in order to predict the mass growth rate of the particle for use in cloud modeling applications. At this

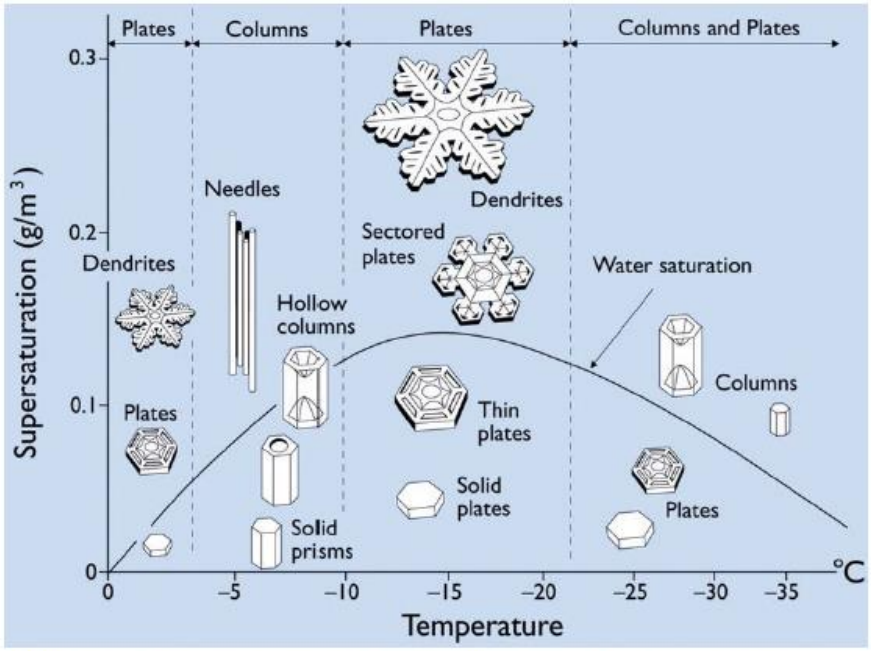

Figure 1.1. The snow crystal morphology diagram depicts conditions in which common ice crystal growth forms are found in the atmosphere. In addition to a strong functional dependence on temperature, the complexity of crystals is proportional to supersaturation (Libbrecht, 2003).

stage, however, it is impossible to model the detailed growth of complex crystals and therefore it is necessary to use simple shapes to describe crystal evolution. Nevertheless, much can be learned by studying the growth of relatively simple single crystals. Models that react according to changes in ambient conditions are crucial for predicting the growth paths of even simple single crystals.

1.1 Ice Crystal Growth Modeling

Currently, the capacitance model is in near-universal use by the cloud modeling community (Pruppacher and Klett, 1997; Meyers et al., 1997; Chiruta and Wang, 2005; Westbrook et al., 2008; Woods et al., 2008). The capacitance growth model is derived from an electrostatic analogy with diffusion; the capacitance acts as an analog to the crystal shape and size. While the capacitance can be computed for any shape (Westbrook

et al., 2008), some models have made use of spheroids as a general approximation for the non-spherical nature of ice crystals (Chen and Lamb, 1994; Hashino and Tripoli, 2007; Harrington et al., 2013a, b). The capacitance model provides only the mass diffusion rate to a non-spherical particle; the model itself does not have a habit generation capability. In fact, the vapor fluxes to the *a*- and *c*-axes from the capacitance model are such that, if they are applied to each axis length, the aspect ratio remains constant in time (e.g. Nelson, 1994; Sulia and Harrington, 2011). Habit evolution requires a method to distribute the gained mass over the crystal.

Traditionally, mass-size relationships derived from in-situ data are utilized to approximate habit development and distribute gained mass over the crystal. Mass gained during growth is presumed to increase the maximum dimension of the ice crystal in accordance to the mass-size relation, and therefore aspect ratio changes are implicitly included in this relation. This method is easily implemented and used in most numerical cloud models, but it does have limitations. In the first place, numerous ice shapes must be used if a cloud model is to cover a reasonable range of possible habit types (e.g. Walko et al., 1995; Woods et al., 2008). In the second place, mass-size relations are traditionally found by fitting curves to aircraft or surface data. However, the entire growth histories of the ice crystals sampled are implicitly included in the mass-size relations, which is inconsistent with the deterministic growth laws.

Mechanistic methods for evolving particle aspect ratios that are rooted in physical theory are arguably preferable to mass-size methods that are largely ad-hoc. However, evolution of the particle aspect ratios requires equations for axis growth rates, but these ultimately depend on the crystal's surface structure, the ambient temperature, and

saturation state (Kuroda and Lacmann, 1982; Nelson and Knight, 1998). Consequently, models that evolve particle axes are typically complex (e.g. Nelson and Baker, 1996; Wood et al., 2001). Simple methods for evolving particle axes do exist (e.g. Cotton, 1972; Demott et al., 1994), but depend on laboratory-determined axis growth rates that are only implicitly tied to fundamental physical properties of the particle.

An alternative method for mechanistically changing the particle aspect ratio that depends on laboratory-determined parameters is the mass distribution hypothesis developed by Chen and Lamb (1994). This hypothesis, Eq. (1.1), assumes that the ratio of the axis growth rates is proportional to the ratio of the deposition coefficients for each axis:

$$\frac{dc}{da} = \frac{\alpha_c(T)}{\alpha_a(T)} \frac{\nabla \rho_c}{\nabla \rho_a} \equiv \Gamma(\mathrm{T})\Phi(\mathrm{c},\mathrm{a}), \tag{1.1}$$

where Φ is the aspect ratio, Γ is the inherent growth ratio, and ρ is the density. In Eq. (1.1) the parameter Φ, or aspect ratio, accounts for the nonspherical shape (or habit) of the crystal. The deposition coefficients (α_c and α_a) are essentially growth efficiencies valued from zero to unity (e.g. Kuroda and Lacmann, 1982) for each axis. Chen and Lamb's (1994) mass distribution hypothesis, when combined with the capacitance growth model, results in a model we refer to as the "adaptive habit model" that is able to capture the changes in the *a*- and *c*-axes over time. The Chen and Lamb (1994) method is able to accurately predict the growth of single ice crystals at liquid saturation. It is noted that due to the complexity of tracking two axis lengths, this method was only recently developed for inclusion within cloud models (e.g. Hashino and Tripoli, 2007; Harrington et al., 2013a and b).

Initial success was achieved when the adaptive habit method of Chen and Lamb (1994) was shown to be in reasonable agreement with laboratory measurements. Additionally, it was demonstrated that simulated ice crystals with aspect ratios near unity demonstrated a shift in primary habit in response to temperature changes that effectively changed the habit regime. This is notable because it demonstrated the feasibility of Chen and Lamb's mass distribution hypothesis. For larger crystals with an aspect ratio far from unity, the initial habit is preserved despite temperature changes (Chen and Lamb, 1994). These features are notable because they adhere to observed crystal properties.

In addition to matching laboratory data, the method of Chen and Lamb (1994) is used as a basis for recent models that predict particle properties instead of using arbitrary ice classes (Hashino and Tripoli, 2007; Morrison and Grabowski, 2008; Harrington et al., 2013a,b). The adaptive habit methodology has been developed into a bulk microphysical model by Harrington et al. (2013a,b) that matches well to binned model simulations (generally within 5%). The creation of a bulk microphysical model that is linked to fundamental laboratory data allows for the immediate incorporation of improvements made to fundamental ice growth databases. While single crystal methods demonstrate the robustness of theory when scrutinized with laboratory results, bulk models allow for a habit evolution method to be incorporated into weather and climate models.

Although the adaptive habit method of Chen and Lamb (1994) is successful, the method is theoretically only valid for diffusion-limited vapor growth. However, growth of ice crystals from the vapor is composed of two related processes: vapor diffusion and surface incorporation of molecules onto the particle. Diffusion limited growth is defined as growth limited by the diffusion rate of water vapor through the surrounding

atmosphere. Near liquid saturation, a common environment where ice crystals grow in mixed phase clouds, growth is entirely diffusion limited; a regime where the adaptive habit method is most suited. As the saturation state decreases below liquid saturation, molecular incorporation can limit the rate at which crystals grow. This is typically called kinetically limited growth, or growth which is limited by the mechanisms required for the attachment of individual vapor molecules to the ice particle surface (see below). Recently, a general theoretical method for including surface-based kinetically limited growth in the adaptive habit model has been developed (the Kinetically Limited Adaptive Habit, KLAH, method; Zhang and Harrington, 2013). This model is advantageous because it can be used directly with laboratory data for single crystal growth.

Surface kinetic resistance is parameterized in models by α (see above), and requires a quantitative model. A theoretical model incorporating kinetic resistance (measured by α) is therefore known as a kinetically limited growth model. It is noted that α is believed to primarily affect habit evolution (mass distribution along the axes) and only indirectly affect growth rates at high saturations (c.f. Chen and Lamb, 1994). At low supersaturations (especially those approaching the critical values), surface incorporation (and therefore low α) greatly reduces growth. Moreover, small particles with sizes (a few microns) near that of the mean free path of a water molecule can have substantially reduced growth rates even when α is near unity (Lamb and Verlinde, 2011, pg. 355). Under these conditions, the approaches of the capacitance and adaptive habit models are not valid (Zhang and Harrington, 2013) and this is important because α can greatly influence cold cloud evolutions. Changing α from a typically used value of 0.5 to a value suggested by laboratory experiments of 0.006 (Magee, 2006) increases ice number

concentration by a factor of 14 (Lohmann et al., 2008). The deposition coefficient was also shown to have strong influence on cirrus dynamics, feeding back into the broader cloud structure and lifetime (Harrington et al., 2009).

Surface kinetic processes differ between the *a*- and *c*-axis (Kuroda and Lacmann, 1982; Wood et al., 2001). Axis-specific growth efficiencies (α_c and α_c) are responsible for the change in primary habit under any conditions; however, the ice surface physics that underlie them are not well understood (Libbrecht, 2003; Libbrecht, 2005).

The KLAH model assumes that the kinetic theory of fluxes determines mass incorporation along the *a*- and *c*-axes at the crystal surface and diffusive (capacitance) fluxes in the far field control the overall flow of vapor mass to the particle. In essence, the KLAH model is a joining of a diffusive growth model for the far field (capacitance) with surface kinetic resistance for the near field. It differs from the traditional spherical model (Lamb and Verlinde, 2011, pg. 354) by applying fluxes independently to model the mass flow of each axis. Despite the decoupled modeling of each axis, this method appears to work well to predict habit-dependent kinetically limited growth (Zhang and Harrington, 2013).

The KLAH model predicts α over time according to ambient conditions based on the critical supersaturation (S_{crit}), which itself depends on temperature (see for instance Nelson and Knight, 1998). S_{crit} represents the minimum supersaturation required to form attachment ledges on the face of a crystal. Currently, values used for S_{crit} were experimentally determined from Libbrecht (2003). Zhang and Harrington (2013) compared the KLAH model to the hexagonal growth model of Wood et al. (2001). This hexagonal model numerically solves diffusion and surface kinetics over a triangular grid

overlaying the particle facets. Results from the comparison indicate that the KLAH model exhibits axis-dependent growth beyond the capabilities of the adaptive habit method of Chen and Lamb (1994) and well beyond that of the capacitance model (Zhang and Harrington, 2013). The KLAH model is able to capture axis-dependent evolution at high and low supersaturations well in comparison to the hexagonal model, a capability that is not possible with the Chen and Lamb (1994) model or the traditional capacitance method. The KLAH model is also sufficiently simple to remain viable for larger scale cloud modeling (unlike the hexagonal model, which is too computationally costly and simulates only solid hexagonal crystals).

One major issue with using axis-dependent growth models of any kind is the lack of laboratory data at temperatures below -22 $^{\circ}$C and at ice supersaturations well below liquid saturation (Harrington et al., 2013b). Here, the lack of data is improved upon by using laboratory measurements taken from the Button Electrode Levitation (BEL) device in conjunction with the new theoretical framework provided by the KLAH model (see Chapter 2). Because the KLAH model is built with few adjustable parameters, it requires only the temperature, ice supersaturation, pressure, and the critical supersaturation as input data. S_{crit}, in turn, can be mechanistically derived from laboratory growth experiments, such as those with the BEL instrument. Further details on the KLAH model and its applications are discussed in Chapter 3.

1.2 Laboratory Measurements

Ice crystal growth chambers exist in many forms, including vacuum devices, wind tunnels, diffusion chambers, and combinations thereof. Particles in these devices are supported by various means, including dynamic air flow, substrates, or electrodynamic levitation.

Extensive use of vacuum chambers by Libbrecht led to the creation of large data sets of growth on substrates (Libbrecht, 2003). Libbrecht (2003) nucleated particles by conditioning compressed nitrogen gas (at 2068 torr) to high saturation and chamber temperature (typically near -10 $^{\circ}$C), then rapidly expanding a small volume into the environmental chamber to cause crystal nucleation. These crystals grew into nearly perfect hexagonal prisms as gravity pulled them to the chamber floor to be recorded on a substrate. These crystals were subsequently transferred by suction into a secondary chamber for growth observations, and temperatures were reduced to experimentally desired temperatures between -15 $^{\circ}$C and -40 $^{\circ}$C. This secondary chamber was evacuated to 2-4 torr to ensure pure water conditions and to prevent vapor diffusion through a gaseous medium (i.e. dry air) from hindering growth (Libbrecht, 2003). Libbrecht's (2003) work provided one of the few sources of deposition coefficient data for kinetically limited conditions (near-zero diffusion) for a large range of temperatures.

Vacuum chamber work was also conducted by Magee et al. (2011) with the Levitating Upper-Tropospheric Environmental Simulator (LUTES) device. Diffusion limited sublimation experiments were conducted with larger (> 20 μm) particles using electrodynamic levitation.

Wind tunnels are most commonly used for suspended large particle growth, such as forming graupel by riming at high saturations (Pflaum and Pruppacher, 1979; von Blohn et al., 2009; Kanji et al., 2011). Single crystals were grown from the vapor by Rodgers (1988) with air conditioned by flow through a diffusion chamber upstream of the growth location. Magee et al. (2006) used electrodynamic levitation to support particles during growth in a slow, conditioned flow wind tunnel. Magee (2006) demonstrated the ability to levitate particles, yet also revealed difficulties in maintaining desired growth conditions. Magee's (2006) work measured the growth (or sublimation) response of one particle over a cycle of temperatures and saturation states. More importantly, it was demonstrated that no single deposition coefficient is able to describe particle growth under changing conditions. This matches theoretical descriptions showing that deposition coefficients depend on supersaturation through the crystal surface structure (e.g. Lamb and Scott, 1974), suggesting a need for deposition coefficient evolution dependent on the environmental conditions. Strong evidence was also found to suggest deposition coefficients were well below unity (about 0.006) at temperatures between -40 $^{\circ}$C and -59 $^{\circ}$C (Magee, 2006). For small particles (less than about 100 μm), ventilation effects are negligible because of the low particle fall velocities (Bailey and Hallett, 2002). Therefore, static diffusion chambers are well suited to growing small single ice crystals in stable, prescribed conditions. For small particles, the enhanced temperature and saturation stability of a diffusion chamber is desirable over flow-driven devices.

Diffusion chamber growth is well documented with devices by Keller (1980), Nelson and Knight (1998), Swanson et al. (1999), Bailey and Hallett (2002, 2004), and Bacon et al. (2003). While the ability to control the conditions inside a diffusion chamber

is well proven, growing a particle in the center of the device is historically wrought with challenges. In order to grow a particle in the region of high supersaturation, glass filaments and tips as well as filaments coated with powdered silver iodide or kaolinite were used as substrates in many studies to support the ice crystals (e.g. Bailey and Hallett, 2002). These studies exhibit uncertainties because substrates may significantly impact growth rates (Libbrecht, 2003). For example, substrates can provide a continuous molecular incorporation ledge source, causing accelerated growth. Electrodynamic levitation eliminates contact (and therefore substrate effects) with the particle through the use of charge repulsion on the z-axis (vertical) and with a stabilizing current in the xy-plane (horizontal). This stabilizing potential has been produced in various ways. For instance, Swanson et al. (1999) used ring-shaped electrodes supplied with alternating current above and below the particle location for lateral stability. These rings produced an electrodynamic potential well, holding the particle in place laterally. The proximity of electrodes to the growing particle proved troublesome, and ice growth accumulations on the electrodes altered the ice supersaturation near the particle (Bacon et al., 2003).

The Button Electrode Levitation (BEL) device was designed to levitate crystals inside a thermal diffusion chamber without interference of the stabilizing electrodes on particle growth. This thereby improved on prior designs such as ring electrodes (e.g. Swanson et al., 1999) and substrates (e.g. Bailey and Hallett, 2002). The BEL chamber was conceived and built to provide insight into the early stages of ice growth. Further details on the development and design of the BEL chamber are discussed in Chapter 2.

Instrument data are invaluable; however, its value is further increased in conjunction with a model that provides a framework for interpreting the results.

Important parameters like the deposition coefficient (α) and critical supersaturations can be derived from the BEL data if used in conjunction with the KLAH model (Zhang and Harrington 2013). The combination of laboratory growth data at temperatures and supersaturations for which data are sparse, along with ice crystal modeling with the KLAH model, will be used in this study to estimate average critical supersaturations (S_{crit}) and deposition coefficients at low temperatures. The KLAH model may also provide insight into the theoretical mechanisms of ice growth (e.g. spiral dislocations or two-dimensional nucleation of attachment sites). Growth mechanisms and analysis of BEL chamber data are discussed in Chapter 3.

Chapter 2

Button Electrode Levitation Diffusion Chamber Description

2.1 Review of Past Techniques and Designs

Measurements of the growth of ice crystals in a laboratory environment emulating cold-cloud temperatures and supersaturations are crucial for improving ice growth knowledge and data required as input for, and corroboration of, ice growth theories including those used in cloud modeling. Laboratory growth chambers allow for precisely controlled growth experiments and observation of ice crystals over time, unlike in situ data. As noted earlier, while in-situ measurements are vital, they provide only a snapshot of ice particles at a particular point in their respective growth history. While such data may be useful for characterizing the structure of clouds and identifying the particles they contain, it is less useful when attempting to understand ice growth processes.

2.1.1 Instrumental Designs

Laboratory ice growth studies were conceived to probe the underlying physics of ice growth in an environment where variables can be tightly constrained. Laboratory crystal growth chambers have been developed in the form of a vacuum device, wind tunnel, and diffusion chamber design.

Vacuum devices confine a growth chamber within a vessel that can be evacuated of atmospheric gas, thus reducing the pressure (and therefore the effects of diffusion, in

the growth region). Pressure reduction is used to both emulate environmental conditions of clouds (e.g. Magee et al., 2011) and to prevent vapor diffusion through a carrier gas from hindering pure vapor growth (e.g. Libbrecht, 2003). Vacuum chambers often require ice crystals to be generated prior to the evacuation of the instrument. The Levitating Upper-Tropospheric Environmental Simulator (LUTES) device was loaded with 10-75μm cylindrical ice particles in a divot located in the center of its levitation electrode. These particles were generated by spraying a fine mist of water into liquid nitrogen. Particle size was limited with a 75μm sieve (Magee et al., 2011). Libbrecht (2003) generated particles by expanding saturated compressed (40 psi) nitrogen gas into a free-fall chamber. The initial chamber was conditioned to growth environments conducive to plates (-15 $^{\circ}$C) or columns (-5 $^{\circ}$C) (Libbrecht, 2003). These particles are allowed to grow in free fall until settling on a substrate. These crystals are transferred into a vacuum chamber by suction onto a second substrate to conduct the primary experiment.

Both devices are evacuated after an existing crystal is inserted. This process is slow, and particles are subject to environmental conditions while the chamber is being reduced in pressure. Particles are not launched directly into their growth regimes; hence it is difficult to control the initial growth or sublimation of the particles.

Wind tunnels are most commonly used to suspend large particles during diffusional or riming (graupel) growth at high saturations (Pflaum and Pruppacher, 1979; Von Blohn, 2009; Kanji et al., 2011). Flow is conditioned upstream of the growth location. For example, Rodgers (1988) grew single particles from the vapor by conditioning the air to specific thermal and vapor conditions by passing the air flow through a diffusion chamber. Wind tunnels are well suited to large particle growth; not

only do they emulate real conditions, but they also contain the ventilation effects experienced by a falling particle. A good example of a modern wind tunnel device built for growth at low saturations is the environmental chamber developed by Magee (2006). While this device was successful in fulfilling its mission, it lacked sufficient control of the supersaturation and temperature it produced. Supersaturation was produced by passing the vertical air flow over frozen coils as it traveled upwards to the growing particle. Ventilation effects are a major advantage of wind tunnel designs. For small particle growths, such as those studied here, ventilation effects are negligible at low fall velocities (Bailey and Hallett, 2002).

Diffusion chambers are well suited to maintaining steady and well characterized growth conditions. Diffusion chamber growth studies have a rich history with devices by Nelson and Knight (1998), Swanson et al. (1999), Bailey and Hallett (2002, 2004), and Bacon et al. (2003). A diffusion chamber is composed of two plates coated with ice to provide a vapor source where the top plate has a higher temperature than the bottom plate. This temperature offset not only maintains thermal stability, but in combination with diffusion it also produces linear gradients of temperature and water vapor in the chamber (hereby known as diffusion theory). Supersaturations in a diffusion chamber can be increased by expanding the temperature difference between the upper and lower plates (e.g. a 5 $^{\circ}$C to a 10 $^{\circ}$C or 15 $^{\circ}$C separation). The greatest temperature difference between the plates produces the largest supersaturation in the chamber center (Figure 2.1).

In review of past designs, the diffusion chamber is most advantageous to this project's goal of small particle growth at low temperatures and supersaturation states

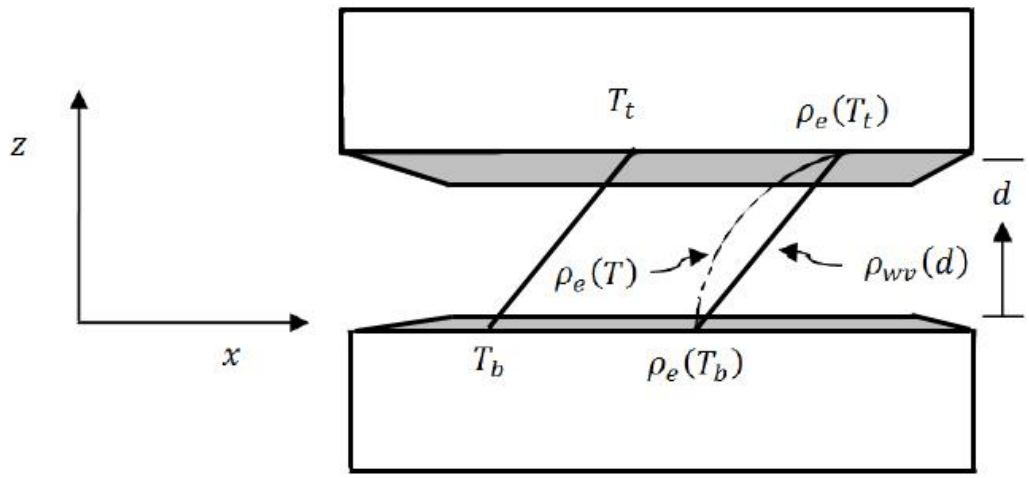

Figure 2.1. Schematic of the supersaturation development in a diffusion chamber. Linear profiles of temperature and vapor pressure produce supersaturation highest near its center. T_t and T_b are the plate temperatures of the top and bottom plate respectively, $\rho_e(T)$ and $\rho_{wv}(T)$ are the saturation and absolute vapor pressure, and d is the plate separation.

ranging from low to high. Wind tunnels lack the control to study particle growth over a range of temperatures and saturations, and vacuum chambers are unsuitable because they are generally inaccessible, require particles to be generated externally to the growth device, and cannot be used at high ice supersaturations. A diffusion chamber provides a consistent environment allowing for long growth periods without drift in environmental conditions. While a diffusion chamber is an ideal design to produce well-defined environmental conditions, a mechanism to hold particles in its saturated center region is also needed.

2.1.2 Particle Levitation and Support

To grow ice in a diffusion chamber, the particle is brought into a central location where supersaturation is developed. In the past, ice crystal growth experiments utilized

substrates such as glass fibers or filaments (Peterson et al., 2010; Bailey and Hallett, 2002). In the case of Bailey and Hallett (2002), crystals were nucleated with a slight adiabatic expansion, allowing for multiple nucleation sites to occur along their glass filament substrate. Multiple crystals competing for growth can be difficult to avoid in the case of substrate nucleation, and vapor competition is likely to be important during the early phases of growth. Substrates may also significantly contribute to altered growth rates (Libbrecht, 2003). While the effects of substrates can be attempted to be removed using theory, it can be difficult to do so in practice. However, substrate effects can be critical as Libbrecht (2003) suggested that substrate interactions produced abnormal growth and that it could potentially increase growth rates as much as a factor of five over substrate-free growth rates (Libbrecht, 2004).

To grow ice particles without substrate interactions, ice particles can be electrically charged prior to growth and be subsequently levitated. Electrodynamic levitation has roots dating back to 1910 when Millikan published his famous Oil Drop Experiment (Millikan, 1911). Millikan's original technique used charged oil drops levitated by a lower charged plate; however, there was no method for providing lateral stability. The first quadrupole trap was developed in 1953 by Paul and Steidwell as an electric mass filter (Davis, 1997). These ideas were modified for growing ice crystals by including a quadrupole composed of four vertically oriented cylindrical electrodes. An alternating current is supplied to the electrodes to stabilize a charged particle, with that particle being levitated by a fifth electrode supplied with direct current of opposite charge than that of the particle (Hu and Makin, 1991; Magee, 2006; Magee et al., 2011). Levitation stability is maintained by adjusting the frequency of the alternating current

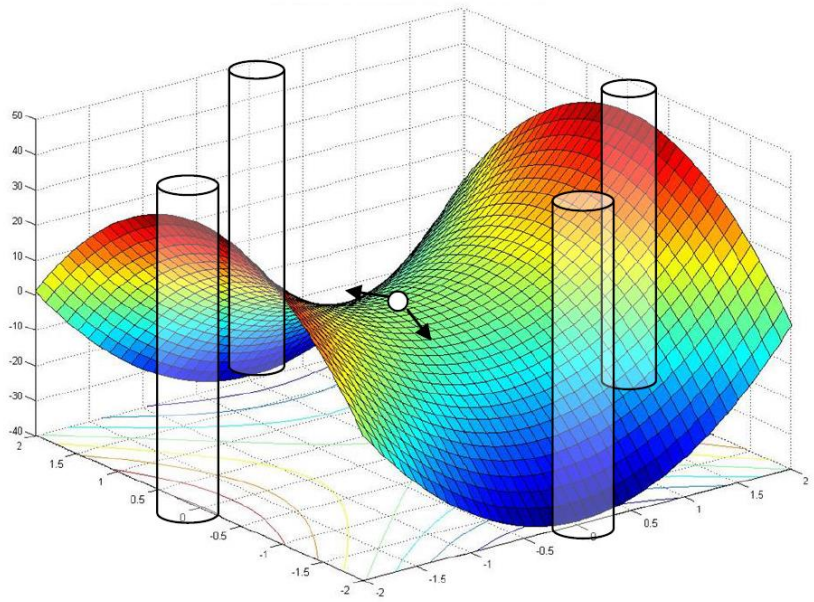

Figure 2.2. The instantaneous three-dimensional potential function for an ideal quadrupole trap. As the "saddle" alternates configuration as the alternating current flips, a hypothetical particle is located at the null point. Arrows indicate instantaneous unstable directions (Davis, 2010).

supplied to the quadrupoles such that the particle maintains its position in the saddle point of the electric field (see Fig 2.2).

Magee's (2006) device used vertical air flow to support the particle from below, while a charged electrode above provided a downward force to levitate the particle and surrounding quadrupole electrodes stabilized the particle. Other levitation devices have been built inside diffusion chambers, such as the ring-based electrode configuration of Swanson et al. (1999). In this configuration, two identical ring electrodes separated by a small amount (3-5 mm) vertically levitate the ice particle against gravity. These ring electrodes are located near the growth region, however, and were problematic. Ice growth was observed on the rings despite an anti-ice coating, creating diffusional interference to the growing particle (Swanson et al., 1999). Unwanted ice growth would also affect a

traditional quadrupole design (e.g. Magee, 2006) if placed in a diffusion chamber. Significant ice accumulation and vapor field disruption would occur, like the growth on the ring electrodes observed by Bacon et al. (2003). Below in Section 2.2, a chamber design (Button Electrode Levitation, or BEL, diffusion chamber) is presented that reduces or removes some of the problematic aspects of prior ice growth experiments.

The merits of electrodynamic levitation are numerous, including the removal of substrate effects and the ability to move particles to different regimes during growth. Electric fields, however, can contribute to significantly enhanced growth. For example, the dendrite in Figure 2.3 demonstrates electrically enhanced tip growth. Dendritic ice tip growth rates have been shown to increase rapidly with increasing electrical potential above a threshold value of between 460 V/cm and 1000 V/cm (Bartlett et al., 1963; Crowther, 1972; Libbrecht and Tanusheva, 1998). It is noted that dendrites are not grown

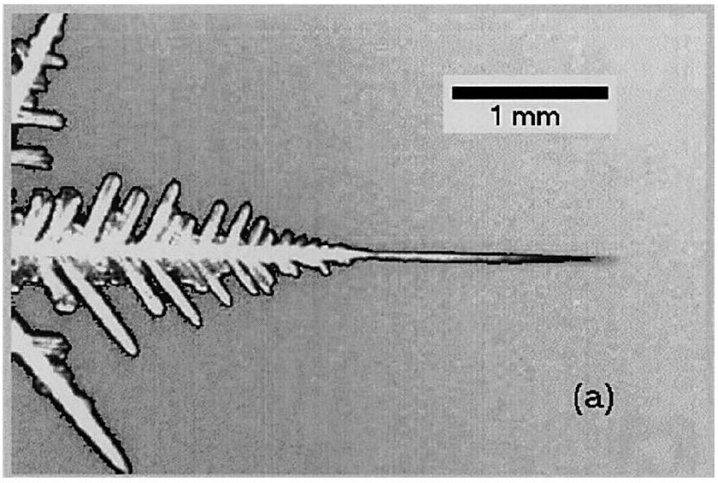

Figure 2.3. An example of electrical enhancement in a dendritic needle. Its growth velocity was observed to increase by a factor of 10 after electric potential was increased over a threshold value (Libbrecht and Tanusheva, 1998).

in this experiment since the particles are likely polycrystalline, and polycrystals do not possess distinct tips where electric potentials can be maximized. (The tips work similarly to a capacitor, and have a very high capacitance).

In the BEL device, ambient direct current fields remain near 100 V/cm, an order of magnitude below the threshold values quoted above (Davis, 2010). Working with a similar electric field, Swanson et al. (1999) showed that an ellipsoidal particle with an aspect ratio of 10:1 would experience a maximum electric field on the order of 240 V/cm. This is also well below the threshold value for enhanced growth. Alternating current fields from the button electrodes produce a larger maximum voltage near 400 V/cm; however, the field experienced by the particle levitating below the electrodes is likely lower (Davis, 2010). This value is still below the minimal threshold value of 460 V/cm. It has also been demonstrated that alternating current fields at 50 Hz do not cause electrically enhanced growth, even with peak fields five times greater than threshold values (Bartlett et al., 1963; Evans, 1973). In a similar experimental setup, Bacon et al. (2003) did not observe morphology changes or dendritic-like growth projections associated with electric effects. Moreover, the results from the studies presented here in Chapter 3 do not show a distinct shift in the particle mass evolution that would occur if the particle growth characteristics changed, as would certainly occur if an electrically enhanced tip were to form. Therefore, it can be tentatively concluded that electrical growth effects are negligible for particles grown in the BEL chamber.

2.2 BEL Chamber Design

The Button Electrode Levitation (BEL) chamber was designed to advance the knowledge of small ice crystal (10 μm to 100 μm) growth at low temperatures (below 243 K). A diffusion chamber based design was chosen for its stability and capability to steadily achieve high supersaturation states. To achieve more accurate growth, electrodynamic levitation was chosen to avoid substrate effects such as those experienced by past designs (e.g. Libbrecht, 2003). Additionally, a design able to remove electrode interference effects on the vapor field in the growth region (e.g. Swanson et al., 1999) was desired. The BEL device was the result of innovating to resolve shortcomings and

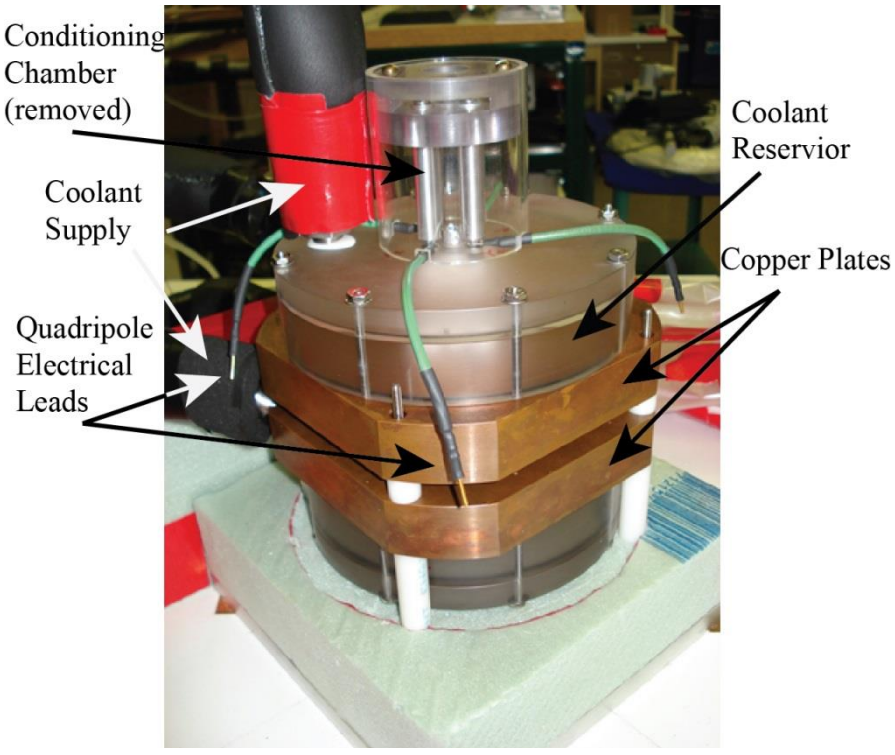

Figure 2.4. Photo of the exterior components of the BEL Chamber without insulation.

limitations of past devices (see Section 2.1.1) and to develop a chamber capable of growing small ice particles at low temperatures and over a range of saturation states. Its design and preparation for use in experiments is described below.

The heart of the BEL diffusion chamber is the levitation system that is a modified version of that used by Magee (2006) and Swanson et al. (1999). In order to remove interference from the quadrupole electrodes in the growth region, the electrodes are reduced to "buttons" extending only 2 mm into the chamber (as seen in Figure 2.5 and 2.6). The button-style electrodes are designed to stabilize levitated particles below the electrodes, therefore allowing the stabilizing quadrupoles to be located above the growth region (in a region of low supersaturation). The button electrodes are insulated from the grounded top plate by 2 mm of Delrin® plastic. In addition to the stabilizing electrodes,

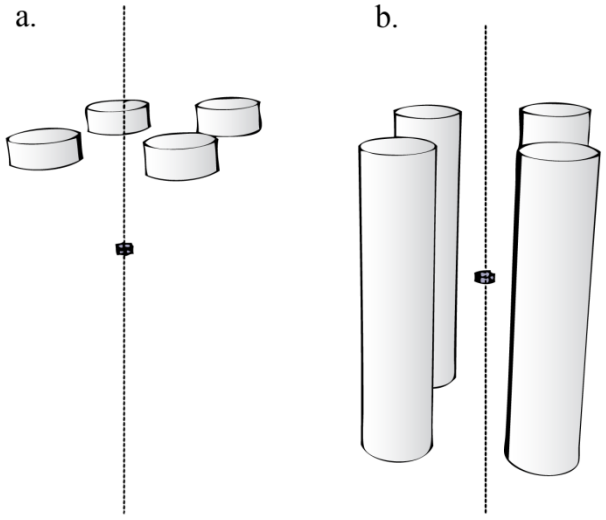

Figure 2.5. Schematic of (a) a "button" electrode configuration and (b) a traditional quadrupole design as used by Magee (2006). The location of the levitated particle is demonstrated by a hexagonal prism.

the bottom plate of the chamber is charged to provide a levitating force counteracting gravity. Together, the bottom plate and button electrodes provide a stable electrodynamic levitation system.

The diffusion chamber is composed of two 2.54 cm thick copper plates that form vertical boundaries of the diffusion chamber (see Figures 2.4, 2.7). Copper was chosen due to its high thermal conductivity, which ensures that the two plates maintain homogeneous temperatures. Cooling power is provided by two Neslab® ULT-95 (Ultra Low Temperature) chillers that circulate fluid (Syltherm®) through two cooling reservoirs attached to the external face of each copper plate (see Figure 2.7). This coolant was chosen due to its low viscosity, which allows it to circulate freely at low temperatures. Each chiller operates independently – one for each plate – and each is capable of cooling a bath to temperatures between -30 $^{\circ}$C and -90 $^{\circ}$C with a temperature stability of +/-0.02 $^{\circ}$C (Thermo Scientific, 2013). The coolant reservoirs are made of cylindrical Plexiglas® with walls secured to the face of the copper plates to maximize the surface area of contact between the plates and the circulating Syltherm® coolant. The coolant flow into the reservoirs is supplied at an angle so that a directionally-induced circulation takes place in each reservoir. This ensures the production of turbulent mixing inside each reservoir, the maintenance of a homogeneous Syltherm® temperature, and consistent coolant contact with the bottom plate (by preventing air bubbles). The moisture source for the diffusion chamber is filter paper wetted with 3mL of filtered deionized water applied to the plate surface. The wet filter paper is applied just as each plate reaches subfreezing temperatures, so the filter paper is held in place by freezing.

Once the vapor source is secure, the chamber is securely closed, and sealed with o-rings to prevent contamination.

The vapor source located at the surface of each plate is determined by the ice equilibrium vapor pressure. Diffusion chamber theory predicts a linear vapor profile, and because the equilibrium vapor pressure varies exponentially with temperature, a supersaturated environment between the plates is produced. Supersaturation in the chamber (hereby referred to as diffusion theory supersaturation) is calculated by

$$\frac{\rho_{wv}(d)}{\rho_e(T(d))}, \tag{2.1}$$

where $\rho_{wv}(d)$ is the theoretical vapor pressure as a function of height (d) in the chamber, and $\rho_e(T(d))$ is equilibrium vapor pressure over ice. Equilibrium vapor pressure calculations were made with a 6th order polynomial fit (Eq. [2.2]) to Wexler's equilibrium vapor pressure expression over ice (Flatau et al., 1991):

$$e_{sat}(T) = a_{1+}a_2(T-T_o)+a_3(T-T_o)^2+a_4(T-T_o)^3+a_5(T-T_o)^4+a_6(T-T_o)^5+a_7(T-T_o)^6. \tag{2.2}$$

In Eq. (2.2), T is the evaluation temperature (in Celsius), T_o is the triple point (273.15 K), and coefficients a_1 through a_7 can be found in Appendix A. Flatau et al.'s (1991) polynomial fit of Wexler's equation is chosen because it is based on more recent experimental data than the equations developed by Goff and Gratch (1946) (hereafter Goff-Gratch).

Ice saturation determination is needed to characterize the growth environment surrounding the particle. The theoretically derived value can also be used to confirm adherence of the chamber to diffusion theory if we compare it to saturations derived from

measurements using sulfuric acid drops of a known composition (e.g. Magee, 2006). However, a gap in the top vapor source is present, because filter paper must be removed to allow for the button electrodes and particle launch opening (see Figure 2.6) and this causes a reduction in vapor flux from the top plate. Consequently, the chamber supersaturation will be lower than predicted by diffusion theory. Deviations from theory will be largest at the center of the chamber due to the lateral diffusion necessary for vapor to diffuse under the vapor gap. Characterization of the chamber using supersaturation derived from equilibrated sulfuric acid drops was also needed to quantify the degree of supersaturation reduction in comparison to diffusion chamber theory. Details on saturation profile characterization are discussed in section 2.5.

Temperature in the growth chamber is determined from diffusion theory, which requires knowledge of the temperatures of the two copper plates. In order to measure the plate temperatures, type T thermocouples are embedded within two millimeters from the interior surfaces of each copper plate. A type T thermocouple (composed of copper and constantan wires) was chosen due to its application range of -200 $^{\circ}$C to 300 $^{\circ}$C

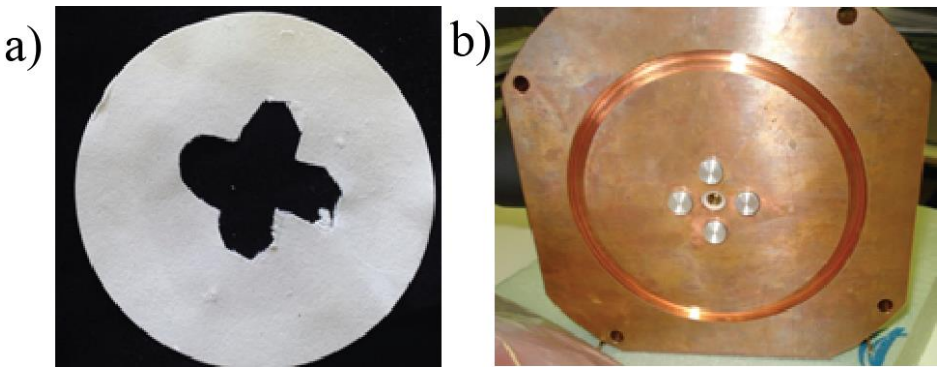

Figure 2.6. Photos of the lid of the BEL chamber demonstrating the extent of the removal of vapor source from vapor source filter paper (a) due to the button electrodes (b).

(Haynes, 2008). Due to the inaccessibility of the interior surface of each copper plate, and to avoid vapor gradient disruptions due to internal thermocouples, embedded thermocouples are the most practical method of temperature measurement. Type T thermocouples measure a voltage differential relative to a known temperature, or reference bath (typically zero degrees Celsius). In order to maintain accuracy, each thermocouple is compared against a zero degree Celsius bath precisely measured by an Omega DP251 precision thermometer.

Copper plates at known temperatures make up the vertical boundaries of the diffusion chamber, and a Plexiglas® ring provides passive lateral walls (see Fig 2.7). Plexiglas® was chosen due to its lack of thermal conductivity and the ease with which windows can be created for viewing inside the chamber. Cellophane is used to seal these

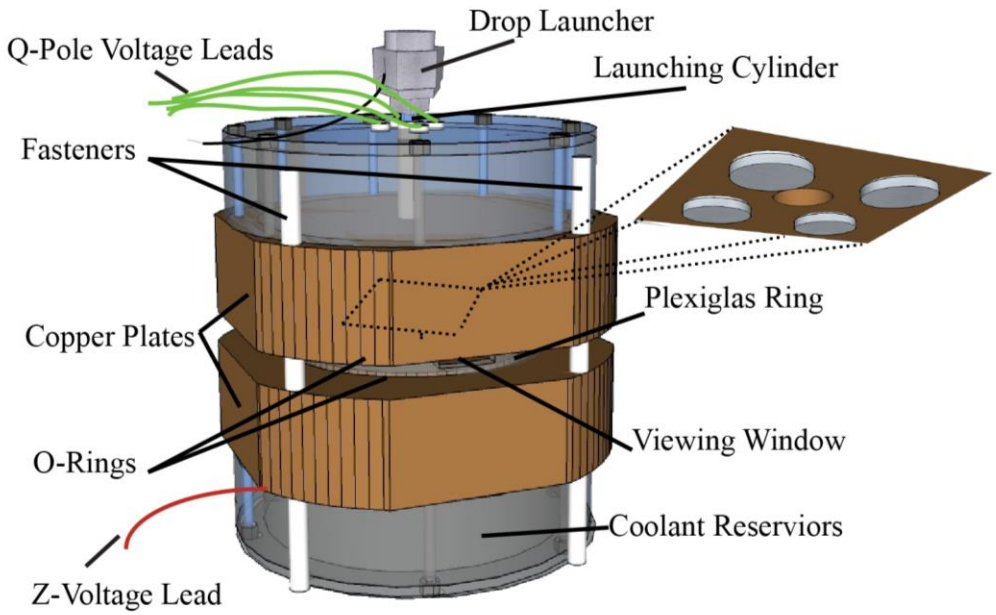

Figure 2.7. Illustration of the BEL chamber design indicating the location and design of its components (coolant supply tubes and insulation are excluded).

windows. The use of cellophane is possible due to the extension of the copper plates beyond the edge of the enclosed chamber, drastically reducing the thermal gradient across the window (see Fig 2.7). Thermal characterization was necessary to confirm temperature profiles inside the diffusion chamber. Results are presented in section 2.4.

Finally, in order to chill each copper plate to temperatures below -30 $^{\circ}$C, the chamber is insulated from the ambient conditions inside the lab. High density home insulation foam 4.85 cm thick was used to encase the entire chamber, helping to consistently maintain the low temperature of the diffusion chamber plates. Thermally, the insulation functions very well; however, ambient moisture in the lab was able to readily permeate the foam enclosure. This caused significant ice accrual on exterior surfaces of the chamber and windows. Ice formations on the windows obstruct the crucial view into the chamber used to track and measure the particle inside (see Appendix B). To remediate ice buildup, the BEL chamber is encapsulated in thin plastic that is provided with a dry air flow having a dew point below -45 $^{\circ}$C, therefore preventing significant ice buildup on the chamber windows.

Further details into the developmental background and design of the BEL chamber can be found in Davis (2011).

2.3 Particle Tracking and Measurement

2.3.1 Particle Tracking

The design of the Button Electrode Levitation (BEL) diffusion chamber limits methods that can be used to access information about the particle growing inside. Microscopes, although they have been used in other studies (Bailey and Hallett, 2004), are not practical with the BEL device. This is in part because the growing particle is not supported by a substrate, and hence rotates rapidly in the quadrupole fields. To obtain information from the growing particle and to track its position, the particle is illuminated with a HeNe laser with a 633 nm wavelength. The illuminated particle is viewed by two cameras looking through windows on opposing edges of the chamber. One camera provides size information while the other tracks, maintains, and records its position.

Maintenance of the exact vertical location of a crystal inside a diffusion chamber is crucial due to the vertical vapor pressure and temperature gradients. Deviation from a particular location results in measurement errors. In order to ensure accurate positioning of particles inside the chamber during experiments, automated tracking software was created. An automated video-based voltage control program was implemented, as suggested by Magee et al. (2011), to improve data sampling for levitated particles. This software is written in MATLAB utilizing the pre-built Data Acquisition Toolbox (DAQ) to control voltage and the Image Acquisition Toolbox (IMAQ) to capture and import camera frames. Pixels from the camera's image (a Point Grey Grasshopper 03K2M) are designated black (background) or white (particle) based on a desired sensitivity. This sensitivity is adjustable to allow for small particle detection as well as reflection filtering

for larger and brighter particles. An example of the sensitivity controls is shown in Fig 2.8. Pixel location is calibrated to z-axis position inside the chamber prior to each experiment by viewing a ruler (graduated to $1/64^{th}$ of an inch and secured in the center of the chamber) through the tracking camera. Consequently, the relative vertical location of each pixel is known with high precision, and maximum errors in vertical location are systematic and on the order of $1/64^{th}$ of an inch.

The particle location is determined by calculating its geometric mean, or centroid, from the generated black and white bitmap. The centroid of a 2D shape is also its center of mass. Centroid tracking was chosen to allow for irregular reflections from the particle to occur without significantly impacting the recorded particle position. This geometric mean supplies a simple, reliable, and automatic measure of the particle location. To maintain the particle position with the software, the desired height in the chamber is chosen along with maximum deviation bounds (see yellow dotted height designation in Figure 2.8a).

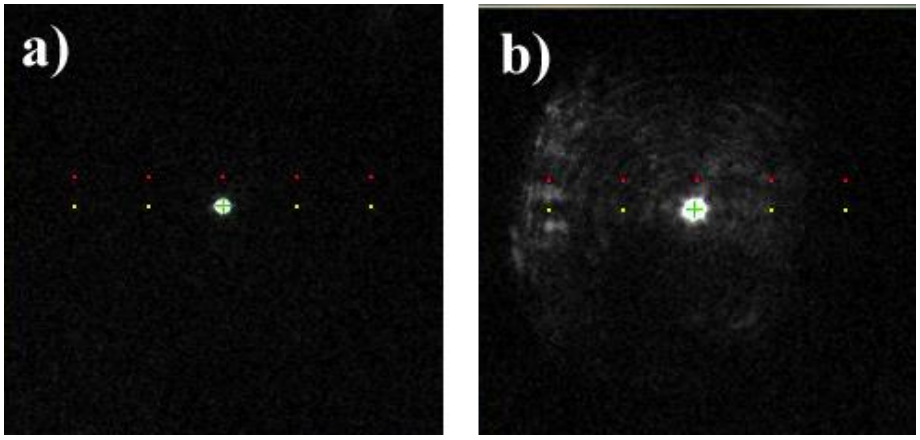

Figure 2.8. Live view of particle tracking (a) during early growth and (b) during later stages of growth. As the particle grows in size, its facets reflect laser light, creating erratic reflections around its true location. By decreasing sensitivity, the particle is sucessfully tracked without detecting any errant light. Software-detected position is visually represented by a green "+",desired particle height is denoted by yellow dots, and a deviation bound (to prevent induced oscillations and to automate particle capture) by red dots.

2.3.2: Automated Particle Control and Recording

The MATLAB software automatically adjusts the particle position, as measured by its centroid viewed on camera (see Section 2.3.1) and by modifying the bottom-plate z-voltage accordingly with a USB PMD-1208FS by Measurement Computing. The PMD-1208FS is a digital to analog converter that translates computer-generated digital signals to analog signals that are receivable by the voltage supply. Voltage is increased when a centroid is detected below the desired growth location, denoted visually as yellow dots in Figure 2.8. Red dots denote a top threshold (or deviation bound) used primarily for particle capture. Particle position (pixel), z-voltage, and a timestamp are recorded for every frame a centroid is detected (up to 30 Hz). The software maintains the centroid's vertical position with an accuracy of 0.1 mm (4 pixels). The tracking camera and the BEL chamber are locked down to the table, ensuring the maintenance of the aforementioned pixel-to-height calibration throughout the experiment.

The particle tracking system is initially calibrated with bare plates. Plate separation does vary slightly due to the application of wet filter paper (surface vapor source of each diffusion chamber boundary). For consistency, 3 mL of deionized water is applied to a new piece of dry filter paper prior to adhesion to the plate surfaces. Any variation in frozen filter paper thickness, albeit slight, is recorded prior to the sealing of the chamber to maintain the accuracy of the particle location above the ice and the plate separation measurement. Height measurements in the chamber are measured from the ice surface, and diffusion theory saturation calculations are adjusted to account for these small deviations. This process ensures an accurate and consistent representation of the particle location in each experiment. It is noted that the steel measurement device is

chilled prior to the thickness measurement in order to prevent irregularities in the ice surface due to melting by contact of the measurement device with the ice surface. If not chilled prior to measurement, the ruler will interrupt the molecularly smooth surface of the ice, thereby creating a region more conducive to vertical ice growth from the bottom plate that may interfere with particle growth at high saturation states.

The particle levitation system works by ensuring that a preexisting charge resides on the particle prior to launch. To allow for electrodynamic levitation, the drop is provided a charge before entry into the chamber. This is accomplished by applying a voltage to the launching apparatus. A voltage-supplying wire is connected to the top of the launcher, as seen in Figure 2.9. Charge is conducted to the water inside the stainless steel enclosure. As a result, drops are launched bearing an initial charge.

The voltage increase of the lower plate to maintain the particle's position is recorded precisely at up to 30 Hz with the MATLAB software. Without automated particle tracking, the precision of the particle location determination decreases

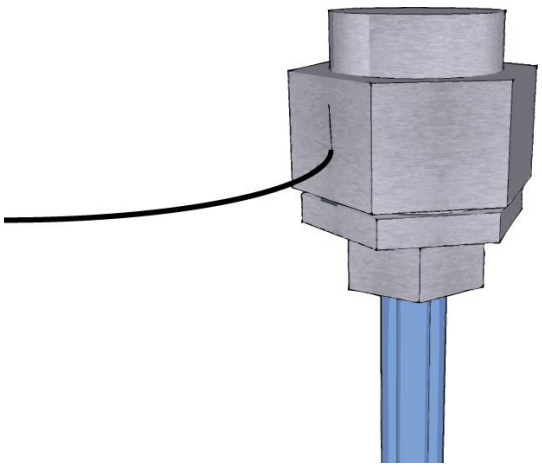

Figure 2.9. A 3-D modeled visualization of the launching apparatus for the BEL chamber. Solution is contained within a glass tube with a 30 micrometer capillary tube embedded in its base (not shown). Charge is applied to the launcher (black wire) to provide particles with the initial charge necessary for electrodynamic levitation.

substantially due to visual voltage adjustments, and data point frequency decreases to 0.02 Hz. The effect of switching from automated to manual control is clearly evident in Figure 2.10, where variability in the mass trace with time is shown. Prior to manual control, the particle growth curve is continuous and well-defined. Once manual control is undertaken, variability in the growth curve is evident due to human-induced errors. Full manual control requires simultaneous z-voltage control, data recording, timer management, quadrupole frequency adjustment, and manual particle positioning: all

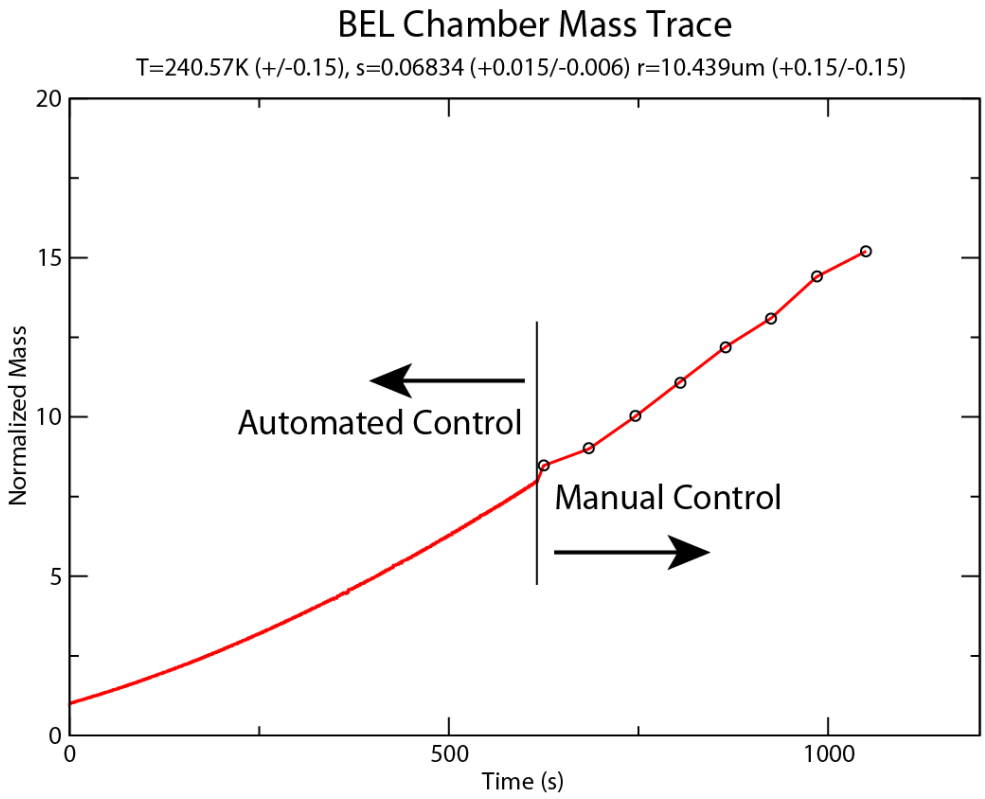

Figure 2.10. Example BEL Chamber growth measurements plotted as a normalized mass (see Section 2.3.3 below). Automated particle control and recording failed midway through the experiment. Manual control was initiated within 5 seconds of failure. Automated control (10,000 data points at up to 30 Hz) provides a high level of detail and resolution versus manual control (8 data points, 0.02 Hz).

potential sources of error and all extremely time-consuming. An automated video-based voltage control program improves the frequency and accuracy of data acquisition and levitation control.

It is noted that elements of manual control exist with the software. The quadrupole frequency must be decreased manually (105 Hz to 15 Hz) as particles grow to maintain a stable saddle point, the voltage step size is increased manually as the particle becomes more massive, and centroid detection sensitivity controls are available to prevent extraneous centroid detection. The effects of these supplemental manual adjustments, however, are minimal, as is evidenced by the lack of any noticeable variability in mass traces that use automated vertical tracking.

2.3.3: Mass Measurements

The z-voltage required to levitate the particle at a constant height inside the chamber provides a measure of the particle's mass. An initial charge is supplied to the launched drop that is great enough to levitate it in the chamber, and this charge remains constant. Consequently, as the particle gains mass, the voltage of the lower plate must be increased to maintain the particle's levitated position. The increase in the lower plate voltage is proportional to the change in the particle mass. Given an initial mass and an initial z-voltage, the normalized mass for the particle can be determined from

$$\frac{\Delta m}{m_0} = \frac{\Delta E}{E_0}, \tag{2.3}$$

and hence a mass trace for the particle can be created, as shown in the figure above.

Particle mass measurement utilizing a charge-to-mass proxy is necessary in part because the "springpoint method" of Magee (2006) is not viable for the BEL chamber. The springpoint method consists of varying the quadrupole frequency until the particle position becomes unstable and begins to oscillate. The oscillation point is distinct and is directly related to the mass of the particle. The small vertical extent of the button electrodes do not allow for a clear instability-inducing frequency (rather a slow loss of stability), hence it is difficult to determine the precise conditions that start the oscillation. Using this method would result in substantial errors in the particle mass that would depend on where the springpoint is defined. Therefore, the springpoint method is not applicable to the BEL chamber (Davis, 2010), and the normalized mass method described above will be used along with Magee's (2006) initial size measurement technique using Mie scattering fringes. Unlike the BEL chamber where the z voltage counteracts only gravity, Magee (2006) was not able to use a direct normalized mass method because vertical airflow was used to balance the particle against gravity.

The growth measurements provide a change in the relative mass. Determination of the actual mass requires knowing the initial mass of the particle, and this can be done using Mie scattering. The real part of the refractive index of water at the laser wavelength used here is well known (1.35) (Schiebener et al., 1990). The angle of scattering into the camera lens (45°) and wavelength of the laser light (633 nm) are known as well. The refractive index is weakly dependent on temperature; however, this variation is negligible over the ranges of temperatures used in this experiment (Schiebener et al., 1990). The result is a well-defined number of Mie fringes per degree that corresponds to a specific particle size, and hence mass.

A Point Grey Grasshopper 03K2M camera captures Mie scattering fringes over a 20° range of angles (35° to 55° forward scattering— a known field of view is necessary for Mie scattering analysis) that is optically directed by a glass lens that enables the camera to capture the entire 20° field of view. Particles must be measured before freezing to obtain well-defined scattering fringes; therefore a high frame rate (30 frames per second, i.e. 30 Hz) is necessary. After processing the Mie fringes, the size of the particle is determined and therefore the initial particle mass is also known. Recorded Mie fringes are manually processed in MATLAB. The number of fringes present in the 20° viewing frame is counted, and the particle size is calculated by comparing the observed number of fringes to numbers from computed Mie scattering fringes generated by a model which has been used successfully in a number of prior experiments (Shaw et al., 2000; Xue et al., 2005; Magee, 2006). These fringe patterns are simulated over the same 20° range ($35\text{-}55^{\circ}$) of forward scattering used in the arrangement of the laser and camera in the experimental configuration. The initial mass of the spherical particle is calculated from this initial size and appropriate density (Haynes, 2008).

Because the voltage supplied to the lower plate required to maintain the particle's position is known, changes in plate voltage during growth are directly related to changes in mass (see Eq. 2.3). Determining mass through a mass-voltage calibration like this is possible because of the constant charge contained on the particle after launch. As mass increases in time, the charge-to-mass ratio on the particle decreases, and a proportional increase to the z-voltage is required to maintain the particle's position. This is only true if the particle does not accrue or lose charge over time. Charge loss and acquisition occur at time scales far longer than experiments performed with the BEL chamber, and were not

observed with sulfuric acid particles levitated for ten hours, which is ten times longer than our experiments. Additionally, particles levitated on a similar system were levitated for days without any appreciable charge loss (Moyle, personal communication). Additionally, charge leakage was determined to be very slow for salt particles levitated for several days in the LUTES device (Magee et al., 2011). Therefore, we have no reason to doubt that normalized mass derived from voltage measurements is an accurate method for measuring the mass of particles inside the BEL chamber.

2.4 Thermal Characterization

Diffusion theory predicts a linear temperature profile within the BEL chamber; however, this is only strictly true if boundary effects can be ignored. The existence of electrodes and cellophane-covered windows may skew the diffusion theory predictions, and therefore it requires confirmation through experiments. Thermal characterization experiments were conducted using the chamber as it would be configured for actual growth studies.

To examine the thermal profile of the BEL chamber, a Type T thermocouple constructed of narrow gauge wire mounted to a small wooden pole was inserted through a slot created in one of the chamber windows. The vertical location of the thermocouple was calibrated using the particle tracking software's pixel calibration capabilities. Resultant temperatures in the center of the chamber (at particle growth location) were measured to be within 1% of diffusion theory. Additional measurements were conducted one inch from the chamber's edge to ensure the presence of a homogeneous environment inside the chamber. Consistent profiles were measured except near the insertion point of

the probe, where a warm bias was present. This anomaly was attributed to small gaps in the seal around the probe allowing ambient air intrusion.

To confirm the thermal properties inside the BEL chamber, two additional calibration experiments were conducted on a fully sealed chamber. Thermocouples were inserted through the particle launch tube (top-down) as well as under the Plexiglas® ring enclosing the chamber (bottom-up). Measurement location was once again vertically calibrated with the particle tracking software. These two methods eliminated the window leakage bias from the initial experiment. Independently, both the top-down and bottom-up methods produced conflicting results (see Figure 2.11). Each method was biased towards the plate to which the thermocouple wire came in contact, thereby creating a warm bias for the top-down method and a cold bias for the bottom-up method. The magnitude of the bias is nearly identical for each method, indicating that the contact of the thermocouple wire with the plates produced the bias. After bias correction, thermal profiles matched diffusion theory and the contact-less lateral thermocouple method to within 1.1% (0.5% in growth location). These results thereby confirm the adherence of the thermal profile inside the BEL chamber to diffusion chamber theory (see Figure 2.11).

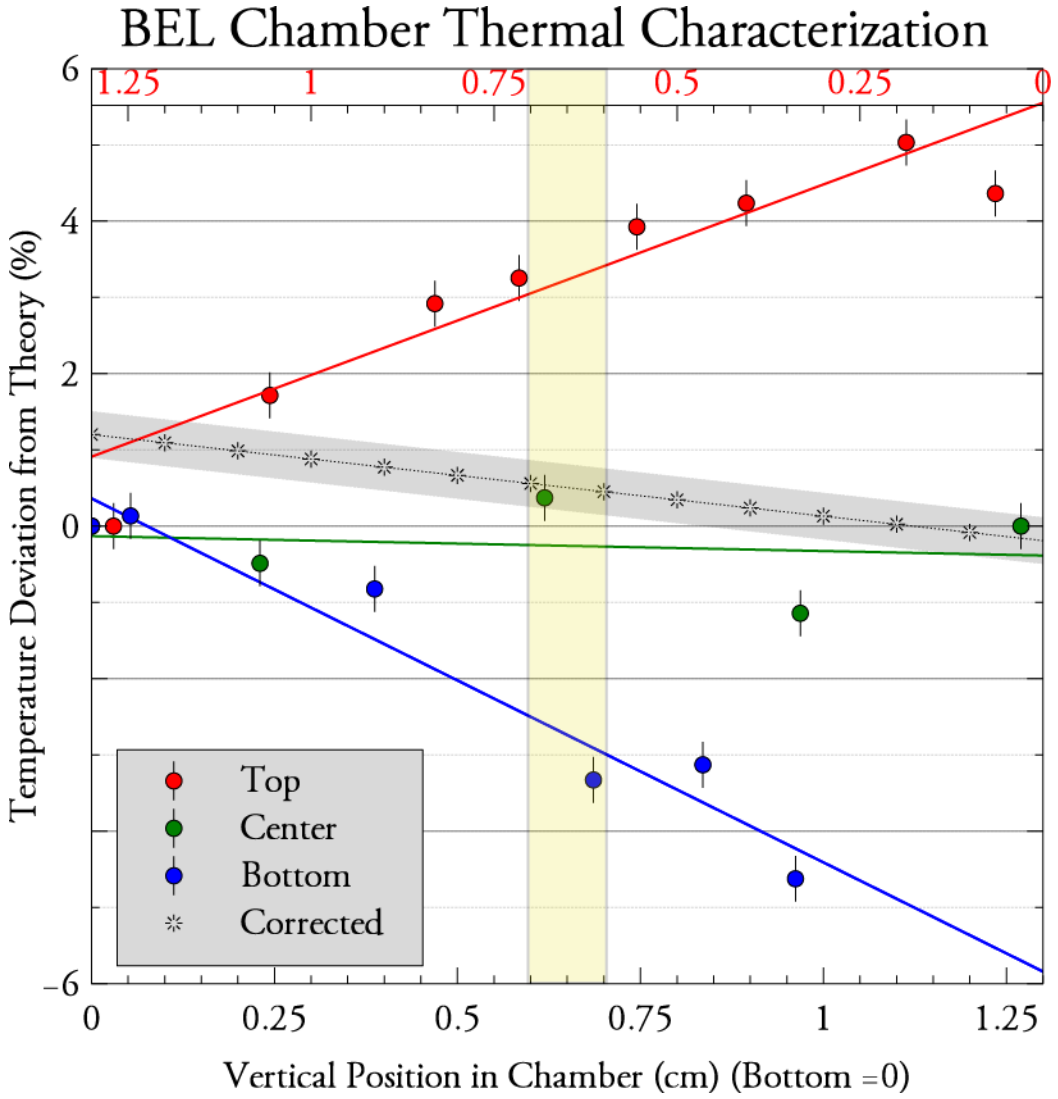

Fig 2.11. Thermal characterization experiments conducted with (red) the top-down, (green) center window, and (blue) bottom-up methods. For the top-down and bottom-up results, vertical position for the top-down case is plotted on the (red) top x-axis and the remaining cases on the (black) bottom x-axis. Bias removal results (*) are plotted as well and the region at which ice growth experiments take place is indicated by the yellow shading.

2.5 Saturation Profile Characterization

Before the BEL chamber is used for growth studies, the vapor pressure profile was characterized by comparing diffusion theory to measurements of supersaturation using equilibrated sulfuric acid drops of known composition. Saturation profile analysis

was notably important for this chamber due to the vapor source gap on the top plate discussed earlier in Section 2.2.

Due to the small dimensions of the chamber, instruments such as a dew point hygrometer cannot be used to measure its saturation state. Magee (2006) utilized a method that combined Mie scattering with Köhler theory for sulfuric acid drops in order to determine the vapor pressure in the chamber. Köhler theory predicts the equilibrium size of a sulfuric acid solution drop for a given humidity, pressure, and temperature. A detailed model of this process was developed by Carslaw et al. (1995) for complex chemical solutions. Requisite information for the Carslaw et al. (1995) model is the molality of the aqueous sulfuric acid solution, temperature, and ambient pressure. Model output is the ambient partial pressure of water vapor, which is converted into a supersaturation value with equilibrium vapor pressures from Flatau et al. (1992). This can be compared to theoretical supersaturation values derived from diffusion theory.

In order to measure the saturation state inside the BEL chamber, the final molality of the acid solution drop levitated inside the chamber was required in addition to the temperature and ambient pressure at the particle location. Particle temperature was derived from diffusion theory (see Section 2.1.1 and 2.4). When a sulfuric acid solution drop is launched into the chamber, it will immediately swell in size depending on the ambient conditions and its concentration. The final molality of the sulfuric acid solution was determined from its initial molality and a measurement of its growth (or swelling). For this experiment, the sulfuric acid solution used is a 4.63 molal (31.4% acid by mass) solution prepared with one part (by volume) pure 18 molar laboratory sulfuric acid and four parts deionized water purified with a Barnstead Nanopure II. This concentration was

chosen to ensure sufficient growth (or swelling) of the acid solution while minimizing acid erosion damage to the instrument.

Measurement of the drop size was accomplished with the same particle tracking system and Mie scattering fringe method used for tracking and sizing water drops. A sulfuric acid drop (4.63 molal) is launched into the chamber and electrodynamically captured. It must immediately pass through the laser-illuminated location in order to capture Mie fringe patterns at its initial size. Images are recorded at 30 Hz to guarantee capture of solution drops at the moment they enter the laser beam. Solution drops that do not fall through the laser beam immediately and launches that produce multiple levitated drops are discarded.

Any gap in time between launch and fringe image capture will result in error. A certain amount of error is unavoidable because there is a finite, though small, amount of time between the sulfuric acid launch and arrival at the laser beam. This error is characterized by considering the first 0.15 s (an estimate of the maximum time between launch and illumination) of growth after initial Mie fringe recording as a maximum error. This estimate is considered the maximum error because the acid drop experiences lower supersaturation, and therefore less growth, in the first 0.15 s before illumination than the 0.15 s after.

The launched sulfuric acid drop is allowed to grow at a fixed location in the chamber until it reaches equilibrium with the surrounding vapor field and stops swelling. This is determined to occur when the particle remains at its location to within 0.03 mm (1 pixel) without requiring any voltage increases for two minutes. At this time, its Mie

scattering fringe pattern is recorded and this is used to determine the particles equilibrium size.

To obtain the final molality of a sulfuric acid drop once it has reached equilibrium with the vapor, a measure of its growth is needed. The initial and final sizes of the suspended drop were determined by Mie theory. Mie scattering fringes were analyzed using a refractive index of 1.388 which is valid for a 35% by mass sulfuric acid and a Helium Neon laser at wavelength of 633 nm near 243 K (Krieger et al. 2000). The refractive index error between the solution used (31.4% by mass) and simulated (35% by mass) was evaluated and considered to be negligible. Additionally, the refractive index of the particle may fall by as much as 0.03 as a result of water adsorption dilution. This was found to cause an uncertainty in sizing of 1% or less. As a result, the size of the 4.63 molal initial drop was measured as well as the size of the final drop of unknown composition. Sizes are determined using the methodology described in section 2.2.3. The growth experienced by the particle is a result of water adsorption into the solution with a fixed mass of sulfuric acid. Because the vapor pressure of sulfuric acid is very low, negligible amounts are lost as vapor, and therefore any additional volume growth by the particle is attributed to water gain. Using radii from the Mie scattering fringe measurements, the volume of the additional water acquired by the particle was calculated, thereby allowing the final molality to be determined.

The vapor pressure in the chamber was then determined from the final molality results with the bulk sulfuric acid solution equilibrium model developed by Carslaw et al. (1995). Experimental temperatures were below 253 K and therefore are well within the range of applicability of the Goff-Gratch equations used by Carslaw et al. (1995).

Sulfuric acid solution morphology is extremely well characterized in the field of chemistry, and therefore the bulk sulfuric acid model is accurate (Carslaw et al., 1995). It is noted that drops smaller than 5 μm are excluded to avoid potential curvature effect errors that are excluded from the bulk models (Carslaw et al., 1995).

Characterization experiments were done over a large range of saturations and temperatures. The temperature in the center of the chamber was varied by setting the bottom plate temperature to between 238 K and 223 K while holding the top plate at 243 K. Supersaturations in the chamber were increased by widening the temperature difference between the upper and lower plates to 5 $^{\circ}$C, 10 $^{\circ}$C and 15 $^{\circ}$C. The greatest temperature difference between the plates produces the greatest supersaturation in the chamber center. Results are displayed in Figure 2.12.

Results from the sulfuric acid drop-based saturation characterization experiments were initially unexpected. In addition to a large variation in the measured supersaturation, measurements were, on average, 42% lower than diffusion theory with a standard deviation of 30.1%. Several results have large deviations from the average, but have been deemed erroneous (i.e. the circled, sub-saturated, and greater than theoretical values) and were excluded. Therefore, a more reasonable range deviation of 20% from the average 42% reduction from diffusion theory is considered the error bounds for this study. The primary rationale for these comprehensive saturation state measurements was that the electrode configuration and launcher location on the upper plate created a vapor source void above the particle location (as described in Section 2.2). In diffusion chamber theory, the entire surface of each plate is a vapor source. The BEL chamber, however, has a symmetrical 2.53 cm diameter region at its center where electrodes are present instead

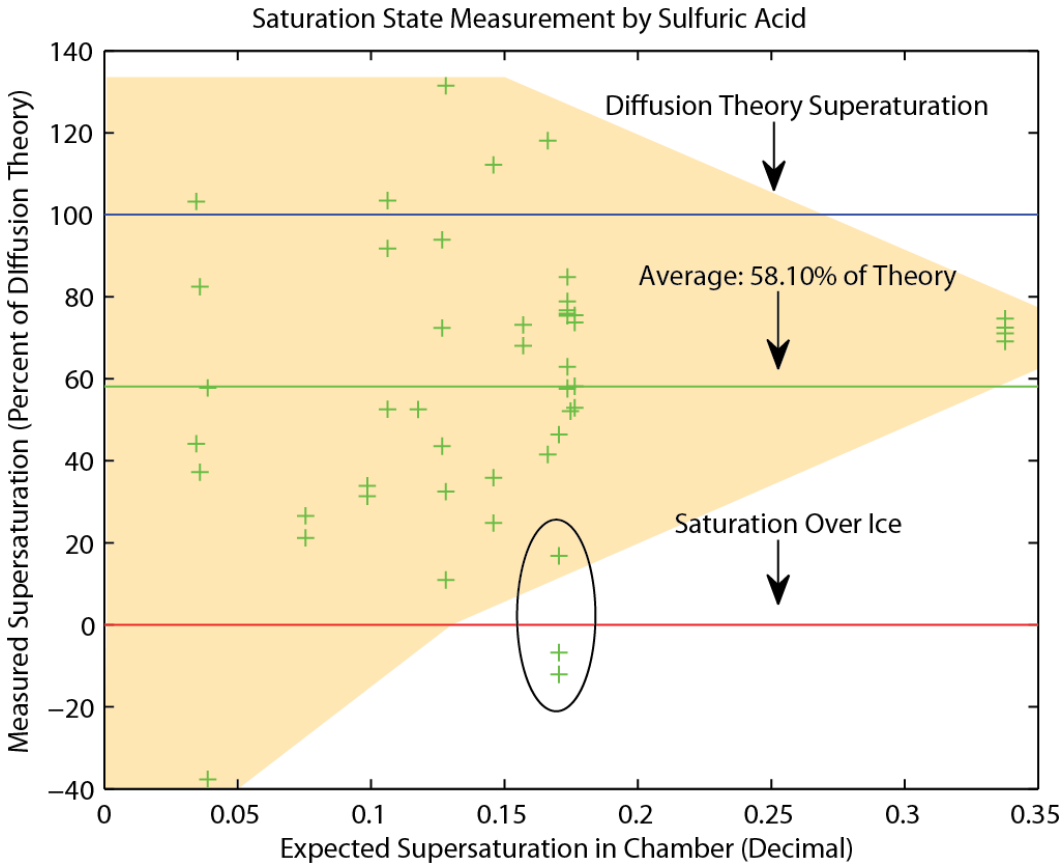

Figure 2.12. Saturation characterization results are plotted individually (green "+"). One "+" represents one sulfuric acid drop launch. The supersaturation of an ideal diffusion chamber (blue), saturation over ice (red), and average experimental supersaturation (green) are also plotted. Experimental saturation state increases left to right. A value of 60 represents 60% of the diffusion theory saturation (60% of the corresponding x-axis value). Shading represents plausible ranges of measured supersaturation. Circled values are suspected to be invalid due to contamination of the vapor source.

of a vapor source. The extent of the vapor source gap is shown in Figure 2.6a. This gap was initially hypothesized to induce a small but consistent negative supersaturation deviation from diffusion theory. This is due to the need for water vapor to also diffuse laterally (as well as vertically) to reach the center of the chamber.

Results from saturation characterization indeed produced a negative deviation from diffusion theory, although a rather large one with a significant standard deviation. An aggregate view of all the measurements produced an average saturation state with

respect to theory (41.9% reduction). It was also evident in the clustering of data points closer to the global average above S_i =0.15 that data precision increases at larger supersaturations. It is noted that a stronger signal (more swelling growth in sulfuric acid drops) is observed for measurements taken at higher supersaturations in the chamber. One exception is three measurements taken at a 17.3% theoretical supersaturation (encircled in Fig 2.12). These data points, all taken during the same experimental series, are suspected to be erroneous due to possible contamination of the vapor source by sulfuric acid. Sulfuric acid contamination of the top filter paper reduces the effectiveness of the vapor source by creating a lower vapor pressure for the resultant solution, thereby decreasing the supersaturation in the chamber.

Although an overall average solution was obtained, individual measurements of chamber saturation exhibit low precision. Large variation in the difference between theoretical and the laboratory results is most pronounced at smaller saturation states below S_i=0.15; however, at this time significant uncertainty is present for all sulfuric acid measurements.

Information can be gathered on the average, but individual saturation results are scattered. These lower precision results may be attributed to the use of small (< 10 μm radius) solution drops as a result of using the same sized launching tips as the water growth experiments for which small drops were desired. Small drops have fewer well-defined Mie scattering fringes than larger drops. This will lead to a weaker signal in fringe changes generated from acid drop swelling, hence more error prone size measurements. In contrast, larger sulfuric acid drops produce a stronger signal through increased numbers of Mie scattering fringes. This is expected to increase the precision of

the measurements, allowing for generation of a more robust saturation characterization of the BEL chamber. It is worth nothing that characterizing supersaturation in diffusion chambers is difficult, and a number of investigators used either diffusion chamber theory, or derived an effective ice supersaturation by minimizing theoretical ice growth curves in comparison to the data (e.g. Bacon et al., 2003).Regardless, our measurements will be revisited using larger solution drops in the future to confirm and improve on current results.

While the temperature in the chamber is well characterized and predicted by diffusion theory, the saturation state is more highly variable and hence uncertain. The variability in saturation state is not atypical of diffusion chamber measurements, and the range of possible errors determined above will be used in the interrogation of the laboratory growth data presented in the next chapter.

Chapter 3

Determining Critical Supersaturation and Deposition Coefficients from BEL Chamber Data

3.1 Introduction

Ice crystal growth from vapor is a complex process because of the formation of largely varied crystal shapes (Bailey and Hallett, 2009) and the many gaps in understanding the physics behind crystal growth (Libbrecht, 2005). The general crystal shape is often characterized by an aspect ratio ($\varphi=c/a$) rooted in the basal (hexagonal) and prism (rectangular) faces of a hexagonal particle. The aspect ratio is a measure of the crystal's primary habit, where a is half the distance across a basal face and c is half the height of a prism face. While temperature appears to define the primary habit of most crystals at temperatures above about -20 $^{\circ}$C, saturation determines the secondary habits of ice crystals (Fletcher, 1973; Bailey and Hallett, 2009). For instance, at temperatures between -12 $^{\circ}$C and -16 $^{\circ}$C, dendritic and stellar crystals form from the underlying hexagonal plate structure. At temperatures near -5 $^{\circ}$C, needle crystals appear as do hollowed columns (see Fig 1.1). Moreover, crystals can take on multiple growth characteristics if they are transported to different growth environments. Plates may grow in one region of a cloud (say at -15 $^{\circ}$C), but columns will grow from the hexagonal ends of the plates if they are advected into a temperature regime where columnar growth dominates (-4 $^{\circ}$C to -9 $^{\circ}$C). For simplicity, the discussion below will be limited to single crystals because polycrystalline ice is more complex.

The difficulty with all theoretical approaches to ice growth is that two problems must be solved: that of surface incorporation, and that of vapor diffusion through "dry" air (primarily molecular nitrogen and oxygen). The details of surface incorporation are not well understood, and so it is typically characterized by a growth efficiency called the deposition coefficient (α) which varies between zero and unity. Habit formation requires the growth efficiency to be different for each axis, as this is the only way that a particle with a non-isometric shape can be produced. Differences in the growth efficiency along each axis influence the diffusion of vapor to the particle, effectively coupling the surface and diffusive processes that control growth (c.f. Libbrecht, 2005; Zhang and Harrington, 2013). The inherent difficulty with solving the combined growth problem is twofold. First, the diffusion problem must be solved for faceted crystals with sharp edges and varied geometries for which no known analytical solutions exist. Second, a model of the deposition coefficient that connects surface incorporation to the supersaturation field above the crystal is required but not yet developed. Difficulties in solving the diffusion problem along with uncertainties regarding how the surface should be modeled naturally lead to the use of simple ice growth models in the atmospheric sciences. Many early models began by forcing the axis growth rates of crystals to be identical to those measured in the lab (e.g. Cotton, 1972; Demott, 1994). Such methods allow multiple crystal axes to grow, but were not mechanistic because the axis growth was fixed, and not dependent on the evolving properties of the crystal. Hence, these methods were limited to specific conditions. In addition, the use of two crystal axes was too complex for most cloud modeling work at that time.

Simplified methods that used only a single axis were developed using the capacitance method as a way to solve the diffusion problem for non-spherical ice. The simplest models used spherical approximations for ice particles with a reduced density, and more complex versions related mass to size with in-situ derived data (e.g. Mitchell, 1994; Walko et al., 1995; Woods et al., 2008). These methods are still generally employed today, both in numerical cloud models and in detailed studies of ice growth. More complete methods were later developed that evolved two axes of a spheroidal model of ice (Chen and Lamb, 1994; Zhang and Harrington, 2013). These frameworks are simplified, yet they allow some freedom for the crystal axes to evolve based on surface physics (see below).

It is only recently that models were developed that included detailed theoretical aspects of ice crystal surface physics, yet are computationally efficient enough to be used for single particle and parcel model studies. The hexagonal growth model of Wood et al. (2001) is one example. This model solves the growth problem by placing a triangular grid over the surface of the basal and prism faces of a hexagonal crystal. Because it is able to model hexagonal shapes through the use of triangular grids, it is a detailed solution that is capable of implementing modern theories for surface incorporation. It is however, still computationally expensive and limited to the growth of a single hexagonal prism crystal. Models (e.g. Zhang and Harrington, 2013) have been developed using parameterizations to match the products of hexagonal models (e.g. Wood et al., 2001) and laboratory data.

Ice growth measurements are confined to the laboratory because in situ data provides only a snapshot of a crystal at a given point in its growth history, and therefore information on the growth rates is not obtainable (Bailey and Hallett, 2009). Past

laboratory datasets have been produced by multiple methodologies including a near-vacuum chamber (diffusion excluded) by Libbrecht (2003), a wind tunnel combined with levitation by Magee (2006), and a diffusion chamber by Swanson et al. (1999) and by Bailey and Hallett (2002, 2004). A vacuum chamber is advantageous for studying surface processes under pure water vapor conditions. In such a situation, the low pressures effectively remove diffusion and it is therefore surface kinetics alone that control growth. However, vacuum chambers are faced with several limitations that include substrate effects and the lack of diffusion (also an advantage) because assumptions must be made in order to extend the measurements to atmospheric conditions. Additionally, observations may only begin after evacuation of the chamber, therefore allowing changes to the particle to occur before the experiment begins. Wind tunnels are most advantageous for riming studies (von Blohn et al., 2009) or the diffusional growth of ice near liquid saturation (Fukuta and Takahashi, 1999; Magee, 2006). Wind tunnels, however, are limited in application because they experience trouble producing high supersaturations at lower temperatures (Magee, 2006). For the purposes of growing an ice crystal from its inception in a stable, well-characterized environment analogous to the atmosphere, a diffusion chamber is ideal.

A diffusion chamber's region of maximum supersaturation is located at the mid-point between its plates, and therefore a particle needs to be stably supported during growth to keep the supersaturation of the environment experienced by the particle constant. In the past, glass fibers have been used as nucleation sites as well as a substrate for growth (Bailey and Hallett, 2002). Substrate effects are suspected of accelerating growth rates initially possibly due to a continuous ledge source at the point of contact

(Libbrecht, 2003). At present, it is not known whether contact with the substrate conditions the crystal in such a way that its later growth is affected. Moreover, when the crystals are relatively small their proximity to each other will affect the vapor fields of their neighbors, and hence their growth. Nevertheless, arguments have been made that growth rates determined after the crystals have become suitably large are not affected by the substrate or neighboring particles. This argument, however, does not apply to the measurement of growth rates for small crystals. Alternatively to substrates, electrodynamic levitation has been used to hold particles in place without electrically enhanced growth being observed (Libbrecht and Tanusheva, 1998; Swanson et al., 1999). The use of such a system with electrodes in the growth region of the diffusion chamber, however, created vapor competition due to unavoidable ice growth on the electrodes (Bacon et al., 2003).

In this study, a new diffusion chamber instrument featuring electrodynamic levitation called the "button electrode levitation" (BEL) chamber is used to grow small (< 15 μm radius) ice crystals. This chamber will serve as a laboratory data source for analysis with and parameter determination for the new kinetically limited adaptive habit (KLAH) model developed by Zhang and Harrington (2013).

3.2 Modeling Methodologies: the KLAH Method

To interrogate and interpret the ice growth data from the laboratory, a model is required. All prior lab studies have used the capacitance model for spherical ice growth modified for constant deposition coefficients following the treatment in Pruppacher and Klett (1997) for liquid drops (e.g. Magee, 2006; Skrotzki et al., 2013). This has been

done despite theoretical ice growth research and careful lab studies suggesting that the deposition coefficient depends on the supersaturation, and that a critical value of the supersaturation typically controls growth (e.g. Lamb and Scott, 1972; Kuroda and Lacmann, 1982; Nelson and Knight, 1998; Libbrecht, 2003). Prior works that have attempted to derive critical supersaturations (and their relations to deposition coefficients) have done so either through vacuum chamber measurements (no diffusion) (Libbrecht, 2003) or through methods that allow the growth of a facet to be detected while the supersaturation is slowly increased (Lamb and Scott, 1972; Nelson and Knight, 1998). A model that connects diffusive growth to the predictions of deposition coefficients based on temperature and supersaturation was not readily available, however, and it was not easily possible to connect deposition coefficients to critical supersaturations.

The Kinetically Limited Adaptive Habit (KLAH) model solves the issues outlined above by connecting the axis-dependent diffusive fluxes along two axes (*a* and *c*) to a model of the deposition coefficient that is dependent on the ambient and critical supersaturations. Therefore, the model is used here because it is uniquely suited to study growth at low supersaturations. Currently, the capacitance model is in near-universal use by the cloud modeling community (Pruppacher and Klett, 1997; Chiruta and Wang, 2005; Meyers et al., 1997; Westbrook et al., 2008; Woods et al., 2008). The capacitance growth model is derived from an electrostatic analogy with diffusion where the capacitance acts as an analog to the crystal shape and size. As long as the capacitance is known, vapor diffusion rates may be rapidly computed. The capacitance is often prescribed for specific conditions as determined in a laboratory (Westbrook et al., 2008; Westbrook and Heymsfield, 2011). The capacitance model for vapor diffusion can be written in the form

$$\frac{dm}{dt} = 4\pi C(c,a) D_v m_w \left[n_\infty - n_{eq}(T_i) \right], \qquad (3.1)$$

where $C(c,a)$ is the capacitance dependent on the particle axes, D_v is the vapor diffusivity, m_w is the molecular mass of water, n_∞ is the far field vapor number density, and $n_{eq}(T_i)$ is the crystal surface equilibrium vapor number density that is dependent on crystal temperature (T_i) (Pruppacher and Klett, 1997, p. 547).

The capacitance model fluxes, however, hold the aspect ratio (φ) constant in time (Nelson, 1994; Sulia and Harrington, 2011). In order to evolve the aspect ratio, Chen and Lamb (1994) followed crystal growth theory and multiplied the capacitance fluxes by α for each axis (α_a and α_c) in a ratio form to produce their mass distribution hypothesis:

$$\frac{dc}{da} = \frac{\alpha_c(T)}{\alpha_a(T)} \frac{\nabla \rho_c}{\nabla \rho_a} \equiv \Gamma(\mathrm{T}) \Phi(\mathrm{c}, \mathrm{a}), \qquad (3.2)$$

where $\Gamma(\mathrm{T}) = \alpha_c/\alpha_a$ is the inherent growth ratio and is assumed to only depend on temperature. This assumption was deemed to be a good assumption from comparisons of habit evolution calculations to laboratory data at liquid saturation (Chen and Lamb, 1994; Sulia and Harrington, 2011).

The addition of surface kinetic resistance to Chen and Lamb's (1994) mass distribution hypothesis is the basis for the KLAH model. The inclusion of surface kinetic resistance for spherical particles was well documented (Lamb and Verlinde, 2011, 331-339) and served as a guide for non-spherical growth. The spherical approach used here divides vapor flow into two regions: a kinetic region within one jump length Δ_v of the surface where surface kinetics limit growth and a continuum region considered to follow diffusion theory (Zhang and Harrington, 2013). The far-field diffusive fluxes provide a

quantity of vapor flow to the crystal while near-field kinetic theory fluxes determine mass distribution along the axes.

Unlike spherical particles, the vapor density around a faceted ice crystal varies with angle around the crystal. In order to account for axes-based growth, the fluxes of a spheroidal crystal along the *a*- and *c*-axes from capacitance theory are modified to include surface kinetic theory. To include surface kinetics, each axis is treated independently and the kinetic theory fluxes are matched to the diffusive fluxes for that axis. This allows for the prediction of the deposition coefficient α, a value between zero (no incorporation) and unity (complete incorporation), for each axis (α_c and α_a,). The deposition coefficients are then used to compute the overall diffusion rate to the particle. Despite the independent calculations of the deposition coefficients for each axis, the growth rates match to those computed with a detailed hexagonal model (Zhang and Harrington, 2013).

The underlying surface physics that control α are not completely understood (Libbrecht, 2005) and so α is often implemented using simplified parameterizations even in detailed models like that of Nelson and Baker (1996). For molecular incorporation, the two most common conceptual models consider the surface to be a continuous source of ledges due to screw dislocations, or molecularly smooth requiring the nucleation of two-dimensional (2D) islands to initiate growth (2D nucleation) (Markov, 2003). These processes are visualized in Figure 3.1. A simple general model for α is the parametric method used in Zhang and Harrington (2013), which originated with Nelson and Baker (1996):

$$\alpha = \left(\frac{S_{\text{local}}}{S_{\text{crit}}}\right)^{m} \tanh\left[\left(\frac{S_{\text{crit}}}{S_{\text{local}}}\right)^{m}\right]. \quad (3.3)$$

In this parameterization, S_{local} is the supersaturation at the crystal surface (also dependent on α), and S_{crit} is the critical supersaturation. It is thought that S_{crit} depends primarily on the crystal surface and the temperature. For 2D nucleation, S_{crit} is the minimum supersaturation required to form 2D islands (Nelson and Baker, 1996). For dislocation growth S_{crit} is not required because a defect is already present on the particle surface, but it provides insight into the range of supersaturation where growth rates increase more rapidly. In Eq. (3.3), the parameter, *m*, is used to roughly differentiate between dislocation and 2D island growth. A value of $m = 1$ produces a continuous rise in α (with normalized S_{local}) consistent with permanent ledges (Burton et al., 1951) while *m* values between 10 and 30 produce a very steep increase in α consistent with 2D

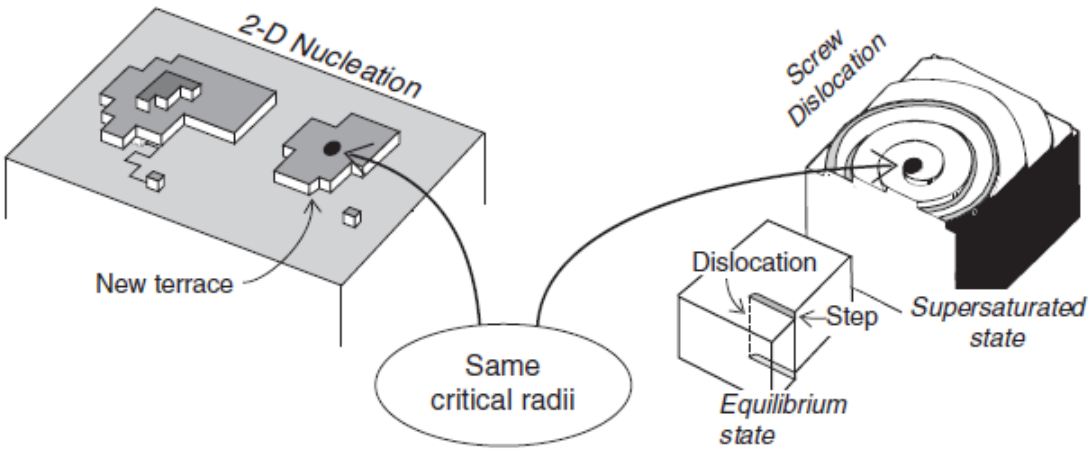

Figure 3.1. Schematic of the surface processes involved in (left) 2D nucleation growth and (right) dislocation growth. In 2D nucleation, islands form on the otherwise molecularly flat surface once a critical supersaturation is reached. For dislocation, growth is steadier and varies in speed based on supersaturation values. (Lamb and Verlinde, 2011, Fig. 8-16)

nucleation growth (Nelson and Baker, 1996). Values of *m* between 1 and 10 have been suggested to describe additional surface types. Zhang and Harrington (2013) used a value of $m = 15$ to derive critical supersaturations from the growth data of Libbrecht (2003).

Experimentally-derived values for S_{crit} are sparse at low temperatures. One source of laboratory data is Libbrecht (2003), where S_{crit} was found to be nearly identical for each crystal facet. In contrast, Zhang and Harrington (2013) derived two S_{crit} values (one for each axis) by using the KLAH model to match α values measured by Libbrecht (2003) following the parametric approach above. This was done with $m = 15$ as the data from Libbrecht (2003) suggest 2D nucleation as the primary growth mechanism at all temperatures. It is important to note the differences in the two approaches. The analysis of Libbrecht (2003) suggests that habit variation occurs through differences in the leading coefficient A(T) for 2D nucleation with Eq. (3.4). This is an alternative parameterization method to Eq. (3.3) in which A(T) was determined to provide the best fit to laboratory data, where

$$\alpha = A(T)\exp(-\frac{S}{S_{crit}}). \tag{3.4}$$

However, the parametric method utilized in the KLAH model (Eq. 3.3) has a leading coefficient that depends on S_{crit} and not A(T), hence habit variation depends only on S_{crit} in this model. While this is inconsistent with Libbrecht's (2003) model, evidence from prior lab studies does suggest that habit variation may depend primarily on S_{crit} (e.g. Lamb and Scott, 1972; Nelson and Knight, 1998). Moreover, the leading coefficient in Libbrecht's (2003) model that controls habit variation is due to the manner by which the data were fitted. Unlike parametric models, and in contrast to classical 2D nucleation

theory, Libbrecht's (2003) deposition coefficients do not asymptotically approach unity as the supersaturation rises. It is the difference in the value to which the growth rates asymptote for each axis that drives habit growth. It is at present unclear whether the axis-dependent deposition coefficients should approach unity at high saturations, or whether they could (in principle) approach a low and constant value as well. Either method can be used in the KLAH model; however, we have used prior parametric approaches (where α asymptotically approaches unity at higher supersaturations) here primarily for consistency with earlier studies. Because we have no method to evaluate the habit that develops in our chamber, we use only a single average value of the critical supersaturation in our studies. Although details on the habit of particles in the chamber are not available, there is strong evidence for facet generation in the form of laser beam reflections recorded from the tracking camera (e.g. Figure 3.2). As prior modeling studies have shown (Zhang and Harrington, 2013), using an average S_{crit} value produces a similar mass evolution to axis-dependent S_{crit} values.

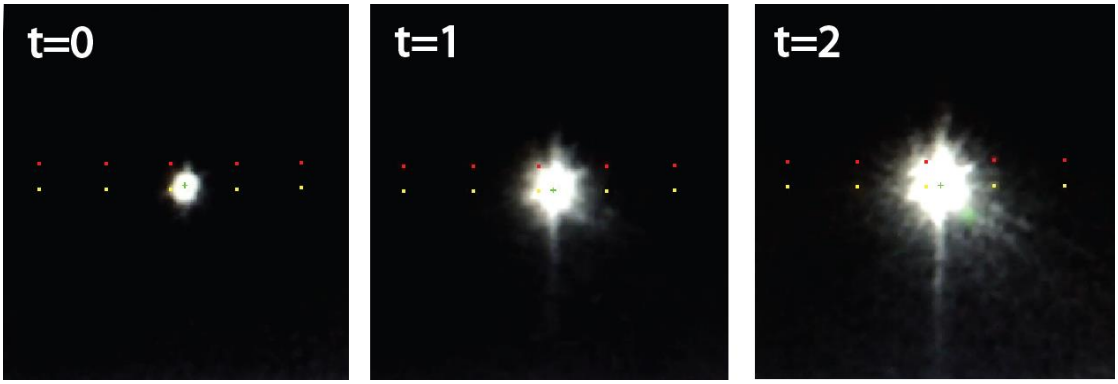

Figure 3.2. The images above of a growing particle in the BEL chamber display evidence of facets. The crystal regularly exhibited "twinkling" up to several times per second as it rotated in levitation.

The KLAH model applies the parameterization in Eq. (3.3) independently to each axis for deposition coefficient prediction during growth. The deposition coefficient, and therefore also mass growth, is strongly dependent on the value of the S_{crit} parameter provided. It is noted that the specific parameterization above is independent of the KLAH method and can be replaced or improved upon with future advances in the understanding of the physics behind α (Zhang and Harrington, 2013). In general, insight into the expected values of α is derived from laboratory data.

Deposition coefficient values are not yet well characterized (e.g. Magee, 2006; Zhang and Harrington 2013). Values of α are dependent on both the environmental temperature and saturation state. Because the surface processes behind α are not yet well understood, laboratory mass growth data provides the best estimates of α (Magee, 2006). Common estimates vary from near unity to 0.006 (Davis, 2011). Magee (2006) produced strong evidence that deposition coefficients for small particles could be as low as 0.006 for low saturations near or below S_{crit}. It is noted that α values derived from laboratory data are not common at temperatures below -30 $^{\circ}$C. Magee (2006) demonstrated that no single deposition coefficient is able to describe particle growth under changing conditions. This suggests a need to examine the evolution of deposition coefficients dependent on environmental conditions, which can be done with the KLAH model.

In order to provide additional insight into α and the initial stages of crystal growth, the KLAH model will be used to analyze growth data from the Button Electrode Levitation (BEL) diffusion chamber device. The determination of parameters (such as S_i and α) relies heavily on fitting laboratory ice growth measurements like those from the BEL instrument. Critical supersaturation values derived from BEL chamber data will be

used to determine KLAH-predicted deposition coefficients over the duration of the crystal's growth.

3.3 BEL Instrument

As discussed above, a diffusion chamber is most advantageous to examining the growth of small particles at low temperatures and over a variety of supersaturation states. A diffusion chamber provides a steady environment that allows for longer growth periods without drift in the environmental conditions. While a diffusion chamber is ideal to produce well-defined environmental conditions, a modified electrodynamic levitation system was needed to grow particles in the supersaturated region of the chamber without vapor interference from the surrounding electrodes that plagued prior designs (e.g. Swanson et al., 1999). The quadrupole electrodes were designed as "buttons" extending only 2 mm below the surface of the top plate to levitate particles below them. These "button" electrodes are located in a region of lower supersaturation far from the particle, preventing substantial ice growth on the electrodes. This electrode configuration leads to the chamber's designation as the Button Electrode Levitation (BEL) device.

The diffusion chamber is composed of two 2.54 cm thick copper plates cooled by attached fluid reservoirs (see Figure 3.3). Syltherm® fluid is circulated into each reservoir and chilled by two NESLAB ULT-95 chillers capable of maintaining temperatures between -30 $^{\circ}$C and -90 $^{\circ}$C with a temperature stability of +/-0.02 $^{\circ}$C (Thermo Scientific, 2013). The chamber is enclosed with a Plexiglas® ring containing

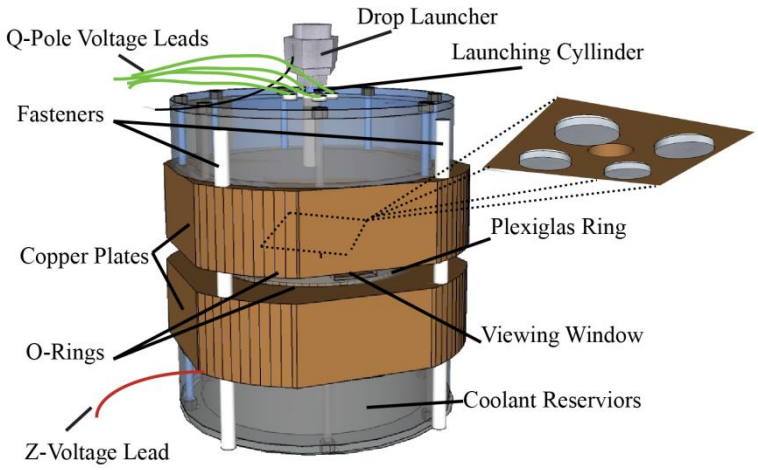

Figure 3.3. Schematic of the BEL diffusion chamber and components.

viewing windows. The copper plates are provided a vapor source in the form of filter paper soaked with 3 mL of filtered deionized water to produce supersaturated conditions in the chamber.

Growth begins by launching small drops (< 15 µm radius) of a 0.2 g/L solution of the bionucleant SNOMAX® (derived from the dead shells of the bacteria *pseudomonas syringae 31A)*. This concentration is chosen to ensure the presence of at least one bacteria shell per 10 µm drop (Bacon et al., 2003). This solution is prepared with deionized water filtered with a Barnstead Nanopure II system to remove any remaining impurities. The SNOMAX® solution is necessary to nucleate ice because pure water will not easily homogenously nucleate above -38 $^{\circ}$C (Lamb and Verlinde, 2011, p. 304).

3.4 Instrumental Data Analysis and Results

3.4.1 Instrumental Data

Due to the long lag time (about 40 minutes) between changing coolant bath temperatures (i.e. Neslab® reservoir) and the thermal equilibration of the plates, it is most feasible to initiate experiments by setting the coolant bath temperature. While this allows for some variation in the plate temperatures (which determine conditions inside the chamber, and hence for analysis), it provides a reasonable, precisely controllable proxy for initiating the experiment. Obtaining a desired plate temperature exactly is a prohibitively long process because a bath set point temperature does not exactly correspond to a final plate temperature, and readjustments are not feasible due to the long lag-time of the plates. At given bath temperatures, plate temperatures are typically 2-3 °C warmer than the baths due to thermal load, and may vary on the order of 1 °C between experiments. It is important to note that these plate temperatures remain steady through the duration of each experimental initialization, each of which typically contains a number of individual ice crystal growths. Differences in plate temperatures exist only between each independent experimental initialization. Even small plate temperature variations can lead to variation in growth temperature and supersaturation among experiments at the same bath temperatures. Therefore, each independent experiment set is evaluated separately from the other sets.

To aid in the analysis and description of the data and results, experiments are divided into three categories of growth experiments where the top bath temperature is -30 °C and the bottom bath is -35 °C (hereafter “3035”), -40 °C (hereafter “3040”), and -

45 °C (hereafter "3045"). Changing the temperature of the lower bath alters the temperature in the chamber, and also leads to an increase in ice supersaturation. Larger variations among experiments in a category are separated into subcategories based on growth conditions (i.e. 3040a, 3040b). This variation is caused by a decrease in one chiller's circulation rates that was discovered and repaired, and therefore this degree of variation is only present for one category. It is important to note that the temperature stability of the plates were unaffected; however a reduced coolant flow resulted in a higher temperature on the bottom plate. Plate temperatures are known to within 0.1 °C, and are constant once plate equilibrium is achieved. Experiments conducted on the same day will maintain the same temperature across multiple growths after initializing the chamber (confirmed between each experiment). Temperature and measured supersaturation (see Chapter 2) conditions for each growth run are provided in Table 3.1.

The measured supersaturation is determined by launching a sulfuric acid droplet of known composition into the chamber at the conclusion of the ice growth experiments, and then using the techniques described in Chapter 2 to derive the supersaturation. The measured saturation state discussed below is considered to be the saturation state estimated from the sulfuric acid-derived characterization results in Chapter 2. The minimum and maximum measured supersaturations are based on the uncertainties associated with determining the sulfuric acid drop composition due to size measurements with Mie scattering fringes. During growth experiments, the saturation state is not expected to vary, and therefore particles complete their growth under one set of conditions. This expectation is based on studies with sulfuric acid drops in equilibrium within the chamber, the size (a measure of saturation state) of which did not vary over a

period of six hours (after reaching a constant size once swelling has ceased). In addition, visible ice accrual was not observed on the interior surfaces of the windows of the chamber. These studies indicate that vapor loss to the windows and interior sides of the chamber had negligible effect on the supersaturation in the chamber, addressing an issue that Skrotzki et al. (2013) noted may have plagued other chambers.

The experimental temperature in the vicinity of the growing ice particle is limited with the current instrumental configuration. The top plate is limited to temperatures of -30 °C and lower due to a limitation with the NESLAB ULT-95 chiller. However, the top plate is also prevented from operating much lower than -30 °C due to the freezing and shattering of the glass launching tips (see Appendix B). Lower temperatures cause water in the tip to freeze faster, causing the launching tip to break before it can be removed from the chamber. As a result of the above limitations, growth experiments are limited to top plate temperatures near -30 °C at this time. A stacked chamber design is being constructed with an upper conditioning chamber to allow for launching at higher temperatures for low temperature growths. The upper chamber can then be used either to pre-condition the particle, or to grow ice particles at a higher temperature. Electrodynamic levitation can then be used to transfer the particle to a lower chamber, the temperature of which can be controlled separately.

In this study, seventeen independent particles were successfully grown in the BEL chamber and growth data were recorded. Mass traces of these particles are shown in Figure 3.4. As expected, the higher saturation states (about 20%, i.e. 3045) led to more rapidly growing ice particles than moderate supersaturations (about 4% to 9%, i.e. 3040a,b), or low saturation states (about 2%, i.e. 3035) that grow at the slowest rate (see

Table 3.1). These three categories (low, moderate, and high supersaturation) form what are termed "characteristic cases" and are the basis of the analysis described further below.

It is worth recalling that temperature is a proxy for ice supersaturation in these studies, hence the lower temperature runs are effectively higher supersaturation runs as well because a larger thermal gradient exists between the lower and upper plates. Future

Measured Conditions (%)				Derived Conditions (%)					Category
S_i	Uncertainty Range		T (°C)	S_i	S_{crit}	Plausible Range (Min->Max)		KLAH factor (f)	
	Min S_i	Max S_i				Min S_{crit}	Max S_{crit}		
2.34	1.93	3.14	-31.48	**4.2**	**3.21**	0.54	1.61	1.5	3035
6.49	5.37	8.72	-32.58	7.6	3.70	1.12	4.14	1.65	3040a
6.49	5.37	8.72	-32.58	8.3	3.92	0.56	4.48	1.75	3040a
9.04	*7.48*	*12.15*	*-33.03*	*6.6*	*2.53*	*4.22*	*8.43*	*0.9*	*3040a*
9.04	*7.48*	*12.15*	*-33.03*	*6.7*	*0.028*	*0.70*	*8.43*	*0.01*	*3040a*
9.04	*7.48*	*12.15*	*-33.03*	*5.4*	*0.98*	*4.22*	*14.05*	*0.35*	*3040a*
1.85	1.53	2.49	-30.87	1.9	0.002	0.002	1.30	0.001	3035
1.85	1.53	2.49	-30.87	1.7	0.2	0.02	1.30	0.1	3035
9.56	7.91	12.84	-33.76	8.55	2.20	1.54	8.80	1	3040a
9.56	7.91	12.84	-33.76	11.7	6.27	0.88	8.36	2.85	3040a
4.01	3.32	5.38	-31.67	5.7	2.88	0.21	2.61	1.38	3040b
4.01	3.32	5.38	-31.67	2.54	1.30	2.61	10.45	0.62	3040b
4.03	3.34	5.42	-31.98	5.2	2.00	0.20	2.40	1	3040b
19.28	15.96	25.91	-35.67	27.9	21.53	3.69	17.96	8.75	3045
19.28	15.96	25.91	-35.67	22.8	15.62	4.92	22.14	6.35	3045
19.28	15.96	25.91	-35.67	21.9	10.45	4.43	19.68	4.25	3045
19.28	15.96	25.91	-35.67	25.1	18.45	4.92	20.42	7.5	3045

Table 3.1. Predicted S_{crit} values and supersaturations for each laboratory ice crystal growth sequence. The left most columns (Measured Conditions) are direct measures of ice supersaturation using levitated sulfuric acid drops, including the likely maximum and minimum based on error analysis. The Derived Conditions columns provide resultant values for critical supersaturation and supersaturation from analysis of laboratory data with the KLAH model (see Section 3.4.2). The plausible range of critical supersaturations represent the upper and lower bounds of plausible S_{crit} values associated with measured uncertainties determined from error analyses (e.g. S_i ranges). Therefore, the range of plausible critical supersaturations may not contain predicted values (i.e. the global minimum, see Section 3.4.2). Shading represents supersaturation values beyond measured ranges, where light shading represents derived supersaturation values above what was measured, light shading with bolding represents values above theoretical supersaturation, and dark shading represents values below what was measured.

studies will explore lower supersaturations at lower temperatures, but those studies will require lowering the upper plate temperature which is not currently feasible (see discussion above). Another present limitation of the BEL chamber is the maximum levitation (or z-axis) voltage achievable by the voltage supply. The maximum z-voltage, in combination with the limited amount of charge on the launched particle, results in a maximum achievable mass that is about 10 to 30-fold greater than the initial mass. Therefore, final particle size is implicit in the instrumental setup. This limitation only affects the length of the dataset, and has no effect on growth measurements.

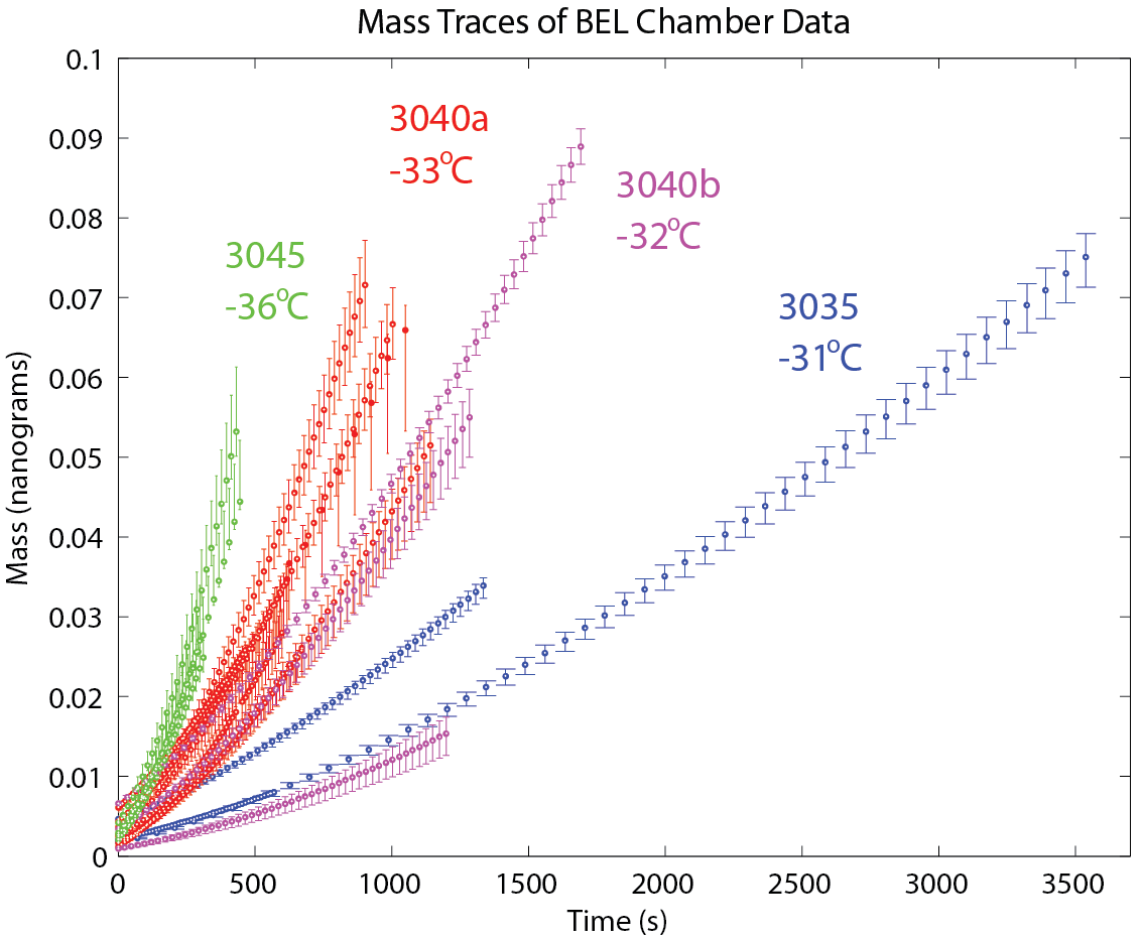

Figure 3.4. Individual particle mass traces divided into low saturation (3035), mid saturation (3040a,b), and high saturation (3045) categories. Temperature labels are approximate for each grouping. Saturation ranges and more detailed growth temperature information are provided in Table 3.1.

For each of the characteristic cases (low, mid, and high supersaturation), the ice crystal growth is modeled explicitly with the KLAH model. Because the KLAH model requires the supersaturation, temperature, pressure, initial size, and the critical supersaturation (and length of growth for comparison to laboratory data), it is reasonable to assume that some combinations of those parameters will lead to the best possible match with the laboratory data. The only quantity above not measured in our studies is the critical supersaturation, which determines particle growth at a given temperature. Hence the goal of our analysis is to determine the critical supersaturations because they are thought to depend primarily on the temperature, and perhaps implicitly on particle size (see Chapter 2). Since the KLAH model predicts the deposition coefficients, we are also able to determine the variation in α with temperature and saturation state.

All of the ambient diffusion chamber conditions are uncertain to some degree. As discussed previously, temperature is known to within about 0.1 K, and so will not produce much error in the growth calculations. Indeed (Strotzki et al., 2013) ignored temperature errors (of 0.3 K) in their analysis for precisely this reason. However, ice supersaturation has significant error associated with it, and there is also some error in the initial particle size. While initial particle size will have some impact, ice supersaturation is by far the greatest source of error when it comes to comparing model and laboratory growth data, as shown below.

Results for the characteristic cases are displayed in Figures 3.5-3.7. The bottom plots in each figure display BEL chamber growth data (black dots) and model simulations (solid or dashed lines). A sparse number of actual data points are plotted because the automated tracking software records particle position and voltage (mass) at a very high

time-resolution. Red lines represent best-fit conditions produced by the model (see discussion in Section 3.4.2); whereas the green and blue curves represent growth calculations using the extremes of the possible ice supersaturation (maximum and minimum, respectively) from supersaturation error analysis (see discussion in Chapter 2). For clarity in presentation, the BEL chamber mass errors (as presented in Fig 3.4) are not displayed. These errors are, however, factored into analysis conducted in section 3.4.2.

In order to quantify the importance of kinetically-limited growth as produced by the KLAH model in comparison to the laboratory data, results are also compared to the predictions of the universally used capacitance model. In Figures 3.5-3.7, the capacitance model, plotted in black, consistently predicts significantly higher growth rates in comparison to the laboratory data and the KLAH model. The deviation between the capacitance model and laboratory data is an order of magnitude larger than the range of errors in the KLAH model estimates as a result of errors in the laboratory data. In fact, even if the plausible ranges of ice supersaturation are used in the capacitance model, that model cannot account for the low rates of growth determined from the data. However, the KLAH model results typically straddle the data using the ranges of supersaturation determined from the chamber. The capacitance model is only able to resemble the laboratory data if supersaturations are far below those determined from the sulfuric acid drop tests. It is clear that considering kinetically limited growth mechanisms is important for growing ice crystals at low temperatures at any saturation state. The capacitance model simply cannot explain the trends in the data, and the KLAH model (which considers kinetically limited growth mechanisms) is able to produce similar growth curves. A thorough discussion of these curves is provided in the next section.

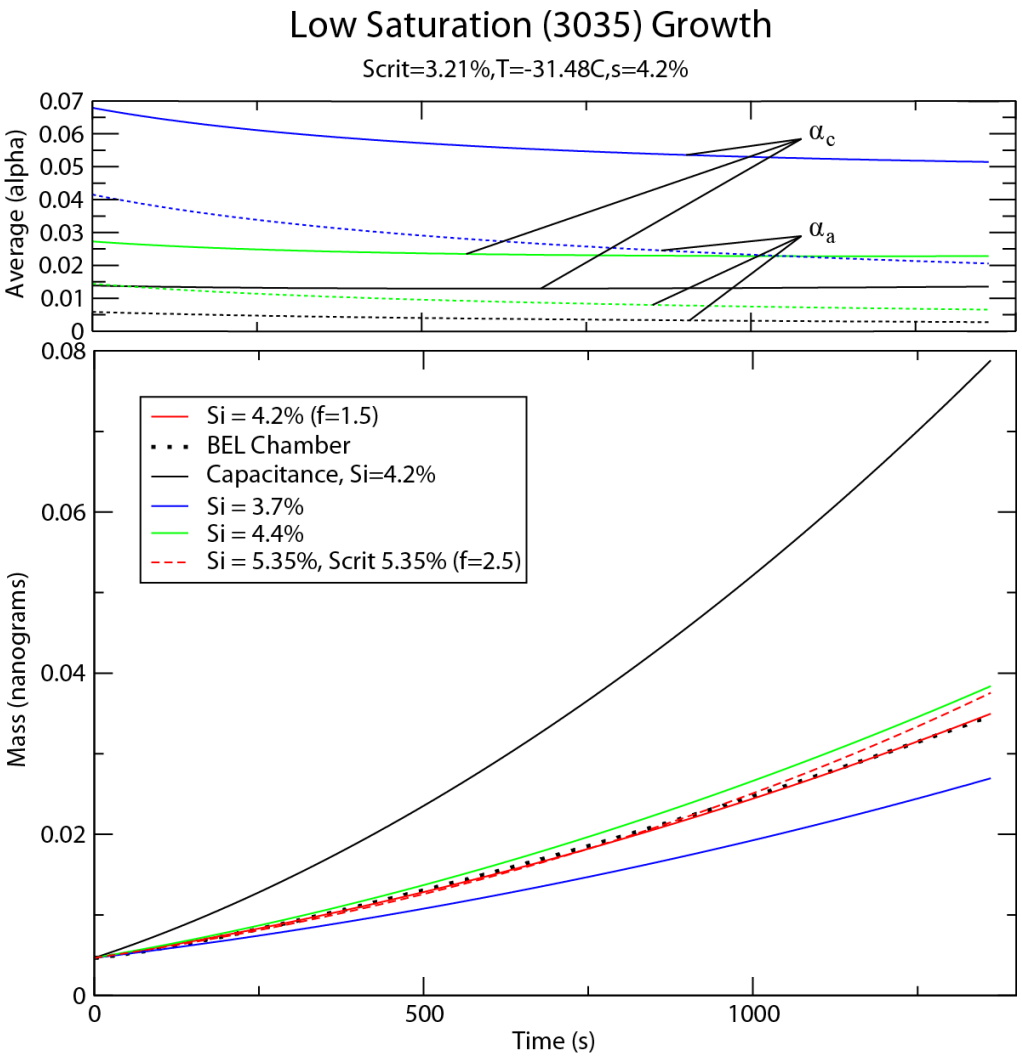

Figure 3.5. (bottom) Growth at two different S_{crit} values (red lines) together with error bounds on the model results that result from minimum (blue line) and maximum (green line) errors in the saturation measurements; capacitance model results are indicated by the black line. (top) Predicted α values for the best model fit to the chamber data are given by the dashed (α_a) and solid (α_c) lines, where colors correspond to the uncertainty bounds of the bottom plot.

The shapes of the predicted growth curves are sensitive to the ambient and critical supersaturation, indicating that minimizing the error between the KLAH model and the laboratory data should allow for a determination of the critical supersaturation and deposition coefficients. Critical supersaturation values determined in this study are single values produced by averaging over the *a*- and *c*-axes. The KLAH model, however,

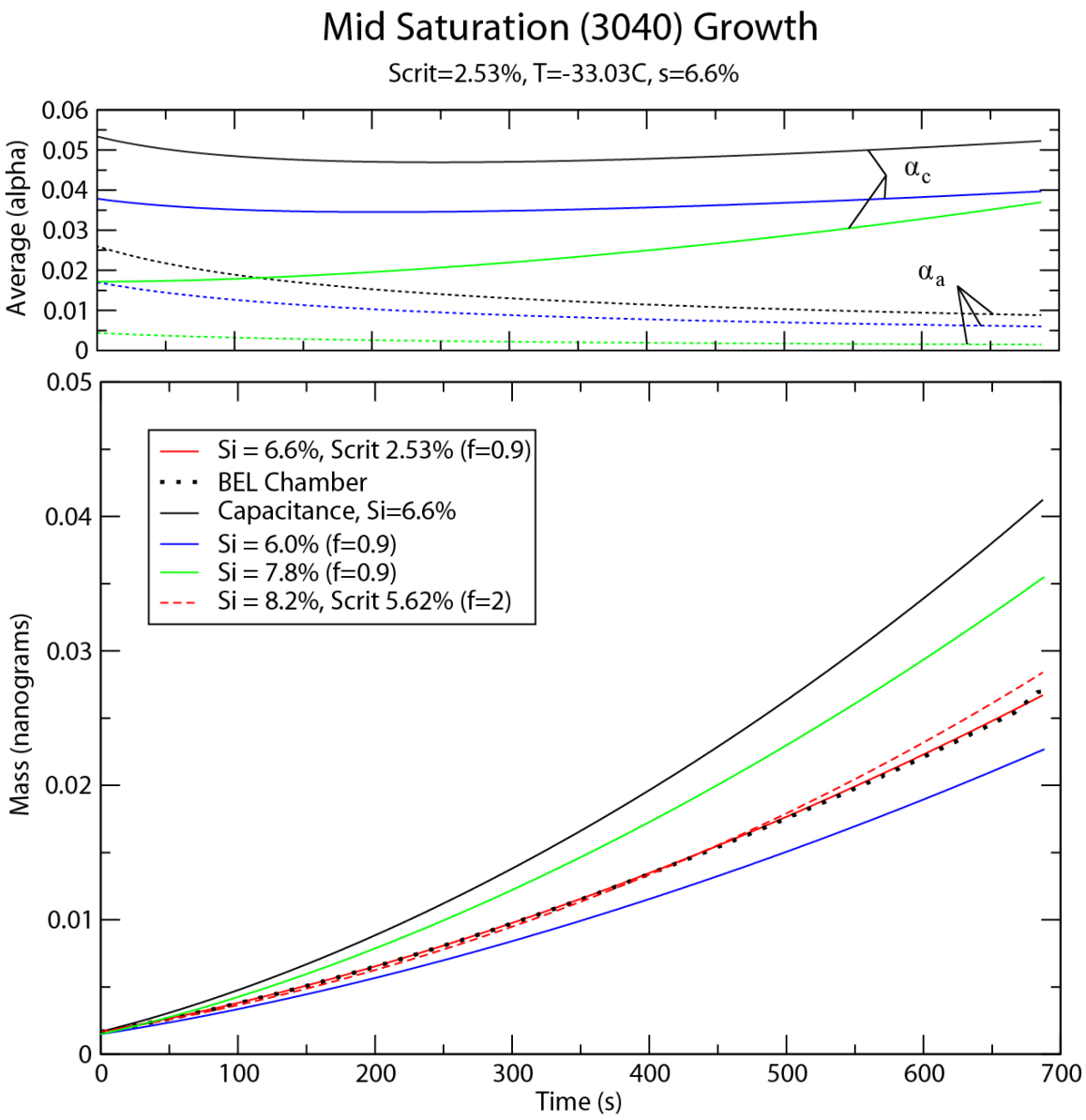

Figure 3.6. (bottom) Growth at two different S_{crit} values (red lines) together with error bounds on the model results that result from minimum (blue line) and maximum (green line) errors in the saturation measurements; capacitance model results are indicated by the black line. (top) Predicted α values for the best model fit to the chamber data are given by the dashed (α_a) and solid (α_c) lines, where colors correspond to the uncertainty bounds of the bottom plot.

utilizes unique S_{crit} values for the *a*- and *c*-axes. To remediate this complexity, the existing critical values used in the KLAH model are adjusted with a factor f. The factor f is the ratio of desired input critical supersaturation to the values originally built into the

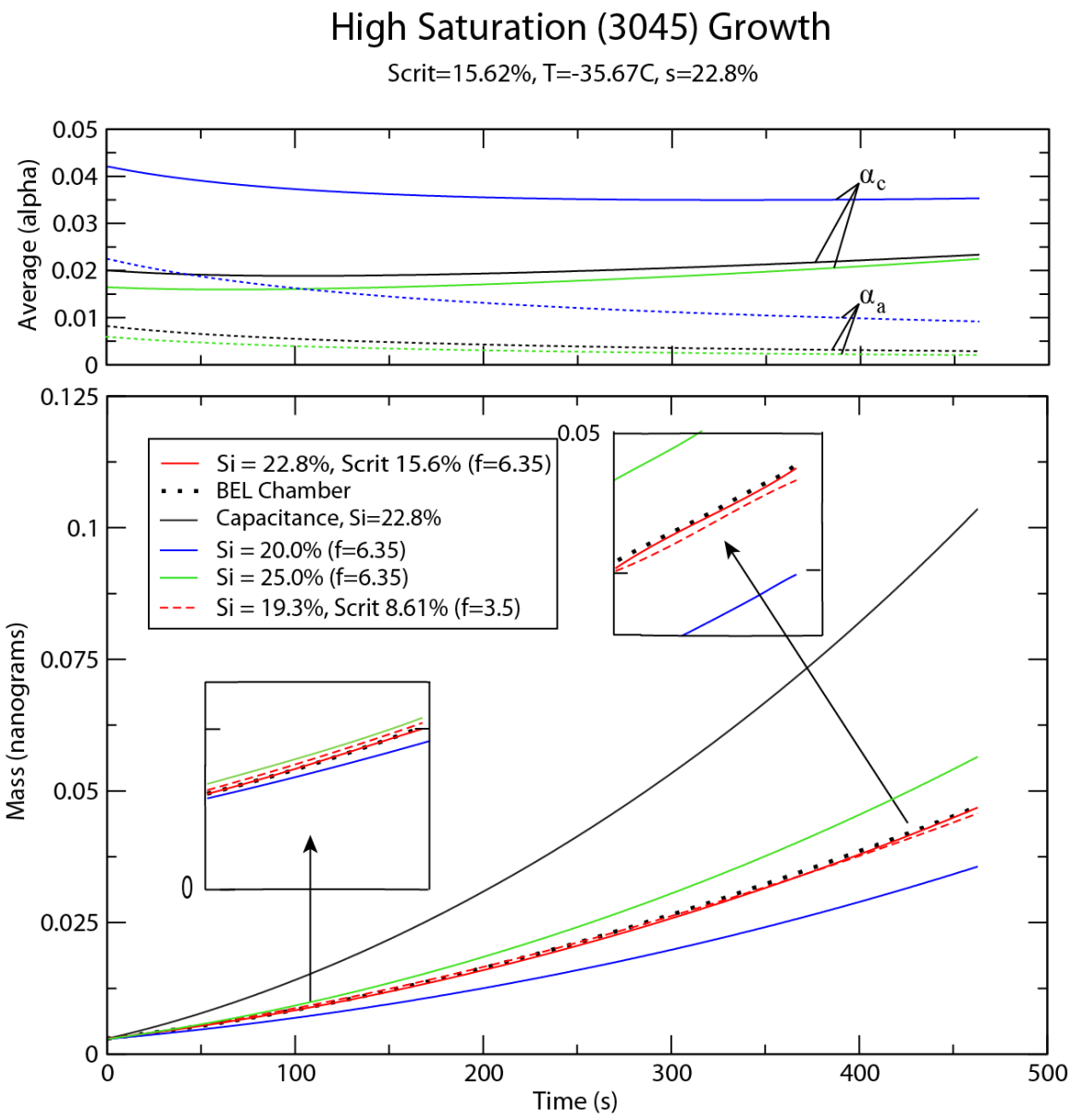

Figure 3.7. (bottom) Growth at two different S_{crit} values (red lines) together with error bounds on the model results that result from minimum (blue line) and maximum (green line) errors in the saturation measurements; capacitance model results are indicated by the black line. (top) Predicted α values for the best model fit to the chamber data are given by the dashed (α_a) and solid (α_c) lines, where colors correspond to the uncertainty bounds of the bottom plot.

KLAH model (hereafter base values). For example, if the base value of axis-averaged S_{crit} is 5% and f = 2, the resultant initialization for the KLAH model would be an axis-averaged S_{crit} value of 10% ($S_{crit,base}$*f). This method maintains the proportionality of S_{crit}

across the *a*- and *c*-axis originally determined from the data of Libbrecht (2003), yet allows for one axis-independent S_{crit} value to be determined.

3.4.2 Critical Supersaturation and Deposition Coefficient Derivation with the KLAH Model

Growth data from the BEL chamber are used to derive (with the KLAH model) the critical supersaturations (and therefore the α's via Eq. 3.3) necessary to reproduce the growth trajectories of laboratory-grown particles. As a result of the automated tracking and control system, data are taken at a high temporal resolution (up to 30 Hz), and therefore only requires minor interpolation during analysis to directly correlate with the model's one second time steps. Because only the critical supersaturations are unknown, a systematic error analysis is used to derive the best fit S_{crit} value for each BEL experiment. To do so, the KLAH model is initialized with a fixed temperature and pressure for each experiment. Because the error in the temperature does not strongly influence the final results, it is not included in our analysis.

As described above S_{crit} is increased or decreased by a fraction, f. For each value of f, the KLAH model is run over an applicable range of supersaturations and a growth curve is produced for each value of the ambient supersaturation. For each curve, a measure of the fit between the laboratory data and the model is produced. The closeness of fit between the model and laboratory data is determined using the relative standard deviation, defined as the square root of the mean of the square of the relative error (to the BEL chamber data) between the KLAH model and the BEL chamber data at each time

step. Hence, for each critical supersaturation fraction, f, an error minimization plot can be produced as a function of the ambient ice supersaturation in the chamber. The conditions at which the KLAH model produces a growth curve most similar to the chamber data coincide with the minimization of the relative standard deviation. Figures 3.8, 3.9, and 3.10 are three examples of error minimization for experiments 3035, 3040, and 3045, respectively. In these figures the x-axis represents the ambient supersaturation for a given model fit to the laboratory data and the y-axis gives the relative error of the fit to the data; each curve in a figure represents a single value for f. Consequently, the minimization procedure provides the set of ambient supersaturation and critical supersaturation values that produce the best fit to the laboratory data. For example, for f=2 the supersaturation that best matches the KLAH model fit to the data is 4%. However, the best model fit to the data does not occur for f=2; it occurs for f=0.1 and a supersaturation of 1.7%. Therefore the global minimum, which is the lowest relative standard deviation produced for a given critical supersaturation and ambient supersaturation pair, is considered to provide the most likely values.

In general, the globally minimized error (lowest minimum) produces the best overall fit to the data; however, other minimizations fit reasonably well and cannot necessarily be discounted as possible solutions (see Figures 3.5-3.7). For instance, small variations in the relative standard deviation can be attributed to initial radius errors in the BEL chamber data. The global minimum in the model fit to the data depends upon the initial mass of the particle, which may contain errors up to 20%. Therefore, a plausible range of S_{crit} values is derived based on the experimentally determined plausible range of measured supersaturations using the sulfuric acid drop experiments in Chapter 2. This

plausible range of supersaturation values is demonstrated by the shading in Figures 3.8-3.10. For instance, the global minimum in Figure 3.8 occurs where f=0.1 and S_i=1.7%, whereas a local minimum for f=0.5 and S_i=2.3% (a value within the plausible range of S_i from sulfuric acid drop measurements) also produces a relatively good fit to laboratory data (see Figures 3.5-3.7). The global minimum may fall outside of this range (e.g. Figure 3.9), which suggests larger errors may be present or a shortcoming of the KLAH model. In such a case, the model required a higher ice supersaturation (~5.7%) than the measured ranged (~3.7-5.5%) in order to produce the best fit with the laboratory data. In order to account for uncertainties in the saturation state, initial radius, and model solutions, a range of possible S_{crit} values are provided. The ranges in measured ambient ice supersaturation can be large due to uncertainties associated with measuring the saturation state inside the chamber (see Chapter 2). However, it is certainly an improvement over other methods that determine the ambient supersaturation through global minimization of model solutions alone (e.g. Swanson et al., 1999). Regardless, reducing these saturation state uncertainties in the future will allow for a reanalysis to narrow S_{crit} ranges.

Global error minimization was completed individually for each set of growth data from all of the seventeen particles grown in the BEL chamber. The model fit that produced the lowest relative error from the BEL chamber data determines the best-fit ambient ice supersaturation and S_{crit} values from the analysis. The resultant supersaturation and S_{crit} information derived from instrument data analysis with the KLAH model (as in Figures 3.8-3.10) is provided in Table 3.1 for all 17 laboratory ice crystal growths. Derived supersaturations fell within the ranges obtained from the sulfuric acid drop supersaturation measurements in 60% of growth cases (unshaded in

Table 3.1), between measured and theoretical values in 12% of growth cases (lightly shaded in Table 3.1), and below the measured values in 24% of growth cases (darkly shaded, bold in Table 3.1). Results in italics represent one set of particle growth experiments that are suspected of being influenced by sulfuric acid contamination of the vapor source which would reduce ambient supersaturation in the chamber. During early experiments, acid drops were launched between particle growth runs to measure the saturation state both before and after the growth of a particle. After evidence of acid contamination of the vapor source (as discussed in Chapter 2), measuring the

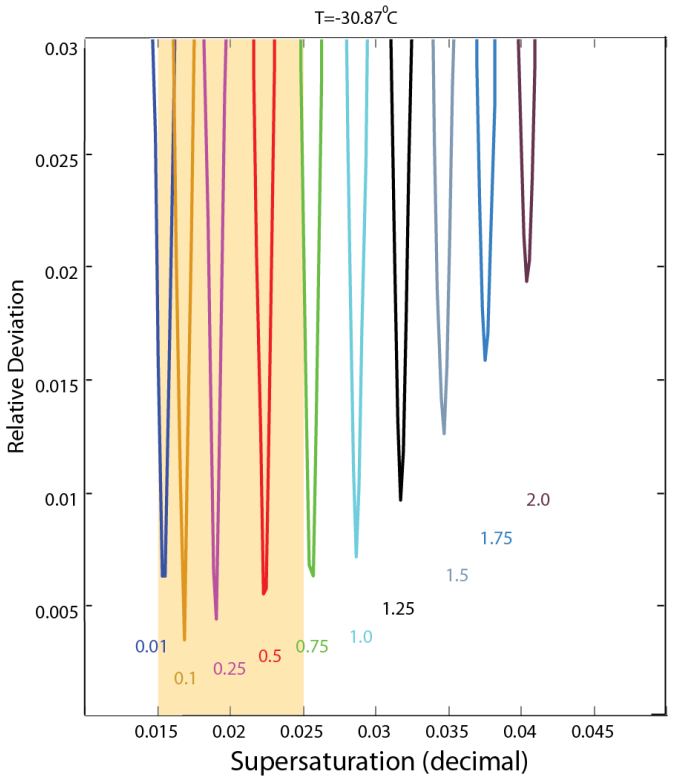

Figure 3.8. KLAH model fit minimization errors for a 3035 case. The color-coded numbers represent the multiplication factor f of predicted S_{crit} over the original KLAH model values. Each curve corresponds to a single Scrit value but multiple supersaturation values as indicated on the x-axis. The error in the fit of the model to the data for each Scrit and supersaturation pair is given by the y-axis. The shaded region represents the range of supersaturations expected as a result of sulfuric acid drop measurement experiments. The temperature at which the ice crystal growth took place is given at the top.

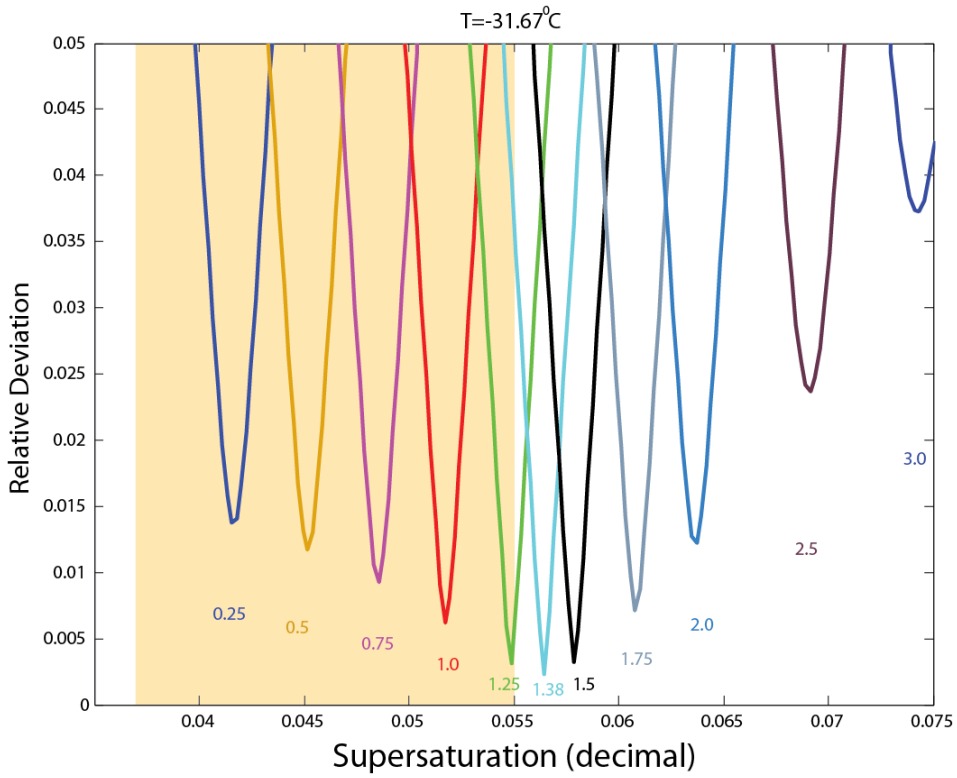

Figure 3.9. KLAH model fit minimization errors for a 3040 case. The color-coded numbers represent the multiplication factor f of predicted S_{crit} over the original KLAH model values. Each curve corresponds to a single Scrit value but multiple supersaturation values as indicated on the x-axis. The error in the fit of the model to the data for each Scrit and supersaturation pair is given by the y-axis. The shaded region represents the range of supersaturations expected as a result of sulfuric acid drop measurement experiments. The temperature at which the ice crystal growth took place is given at the top.

supersaturation with sulfuric acid drops was confined to after all ice growth runs were completed for that experimental initialization. This procedure is not expected to pose any serious problems because experiments with sulfuric acid drops indicate that the supersaturation remains steady over time-periods that are much longer than our growth studies (see Chapter 2). Because critical supersaturation values derived from the chamber are used to predict α (Eq. 3.3), it is imperative to directly analyze how chamber errors may influence the results produced by the KLAH model.

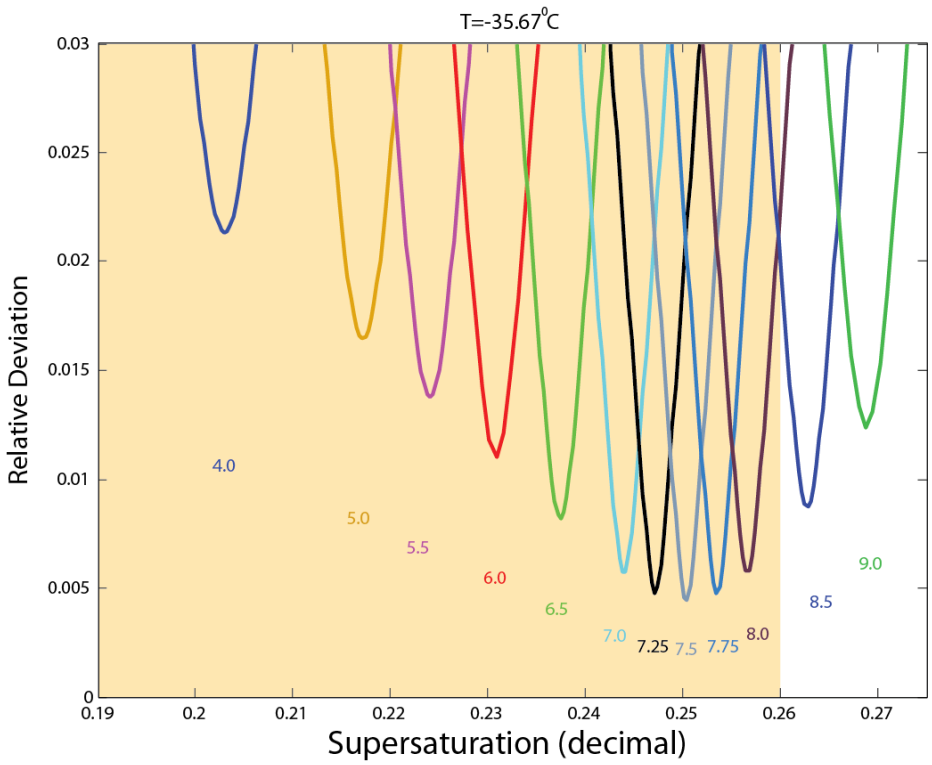

Figure 3.10. KLAH model fit minimization errors for a 3045 case. The color-coded numbers represent the multiplication factor f of predicted S_{crit} over the original KLAH model values. Each curve corresponds to a single Scrit value but multiple supersaturation values as indicated on the x-axis. The error in the fit of the model to the data for each Scrit and supersaturation pair is given by the y-axis. The shaded region represents the range of supersaturations expected as a result of sulfuric acid drop measurement experiments. The temperature at which the ice crystal growth took place is given at the top.

The best fit S_{crit} values obtained above are subject to two main sources of error: initial mass and chamber supersaturation measurement errors. The mass of the particle at any time is determined by its initial mass and then increments in the mass that are proportional with the voltage increases. This provides reasonably accurate estimates of the mass increases during growth as long as the particle does not leach charge during the experiment. Tests with sulfuric acid drops indicate that our apparatus does not cause charge leakage in any detectable amount (Chapter 2). Errors in the initial mass stem from measuring the initial size of the particle, which is accurate to within 1 μm radius (see

Chapter 2). This error is greater at lower temperatures because sizing is only possible with a liquid drop. The drop freezes more quickly at lower temperatures, thereby creating a gap in time between the initial size measurement and initialization of data collection. Time is required to remove the launcher, and data cannot be collected prior to launcher removal because the launcher tip is charged. The charged tip creates a residual force on the particle from above, causing a bias in the mass of the drop because the mass is no longer directly correlated with the bottom plate voltage required to levitate it. At higher temperatures, sufficient time is available to remove the launcher prior to collecting growth data. Resultant maximum errors in derived S_{crit} are on the order of +/-20% for low and mid saturations and -10/+50% for high saturations. Underestimation (overestimation) of the initial ice crystal radius results in an underestimation (overestimation) of the final S_{crit}. Uncertainty in the saturation state (-0.6/+1.5% in S_i individually, or a +/-20% deviation aggregately, see Chapter 2) provides a range of S_{crit} values which best fit the BEL chamber data (e.g. ranges in Figures 3.8-3.10).

In order to analyze the effects of S_{crit} on ice growth in the KLAH model, mass traces from different S_{crit} values are plotted at the conditions corresponding to the best-fit values (see Figures 3.5-3.7). It is clear in Figures 3.5 and 3.6 (Figure 3.7) that a larger (smaller) S_{crit} value at its best-fit supersaturation grows a particle too slowly (quickly) at first, but too quickly (slowly) later. The modeled growth at the conditions derived from the minimization of relative deviation (solid red line) clearly produces the best fit to laboratory data (black dots). The evidence of a change in the shape of the growth curves suggests that the S_{crit} values obtained here are robust for best-fit conditions.

It is important to note that the shape of the laboratory growth curves can only be reproduced with kinetically-limited growth and that the curve shape depends on the critical supersaturation assumed. For instance, Figure 3.5 shows that for an ambient supersaturation of 4.2% and a critical supersaturation of 3.21%, the match between the laboratory growth data and the KLAH model is excellent and produces the lowest relative error. However, a supersaturation of 5.35% requires a critical supersaturation of 5.35% for a best-match with the laboratory data. In this case, the match with the laboratory data is quite good initially, but the curves diverge towards the end of the simulation. This result indicates that feedback between surface-kinetics and diffusion alter the growth rates and the shape of the growth curves. In the case shown here, a higher critical supersaturation requires a higher ambient ice supersaturation for the initial growth of the ice particle to match the data. However, as that particle grows larger, diffusive processes become more important, and the growth rate accelerates because of the larger supersaturation, resulting in a growth curve that deviates from the laboratory data. This effect is also present for cases that require a lower S_{crit} (e.g. Figure 3.7) because growth occurs more rapidly initially but at a lower ambient supersaturation; therefore, the particle experiences slower growth once diffusive processes become more important. The other growth experiments share these characteristics in common. It is critical to note that these results indicate that a single value of the deposition coefficient cannot produce the correct growth curve shape, as previously pointed out by Magee et al. (2006). If the deposition coefficients were constant, then the growth curves would all retain the same basic shape.

The deposition coefficients shown in Figures 3.5-3.7 as solid lines are those derived from the best match between the KLAH model and laboratory growth data used to determine S_{crit} above. For instance, Figure 3.5 shows deposition coefficients resulting from an ambient supersaturation of 4.2% and a critical supersaturation of 3.21%. In order to account for uncertainty in the initial particle size and ambient supersaturation, simulations with the KLAH model are completed using the extremes of the error bounds: minimum (maximum) radius and maximum (minimum) supersaturation. It is noted that derived α values (see Section 3.4.2 for details) exhibit some general trends. For instance, the deposition coefficients decrease in time in general. This is an expected result as Sheridan (2008) showed that the local supersaturation over a growing crystal decreases as the particle grows larger, and therefore the deposition coefficient should decrease. Nevertheless, the uncertainties in initial size and supersaturation lead to a range of possible deposition coefficients, though the values are all typically small.

In addition to the predicted axis-dependent α (α_c and α_a) and associated uncertainty displayed in Figures 3.5-3.7 for select cases, the average α derived for each particle is provided in Table 3.2. In a few cases, the average values do not fall within their maximum and minimum bounds based on saturation and initial ice crystal size errors; this occurs when the global minimization occurs outside of the measured saturation range. The rationale behind this is discussed earlier in the chapter. In general, the deposition coefficients predicted here are lower than 0.16, and most results fall on average below 0.08. A majority of growth runs resulted in a predicted average α of below 0.05. This suggests α values approaching those suggested by Magee (2006) ranging from as low as 0.006 for a particle at -40 °C (colder than these experiments) and low

saturation. The plausibility of low α values is also suggested by Gierens et al. (2003). Only one of our laboratory growth runs reaches the deposition coefficients (typically greater than 0.1) determined by Strotzki et al. (2013). This is critical because deposition coefficients below 0.1 typically produce kinetic limitations to growth that substantially deviate from classical diffusion theory (e.g. Gierens et al., 2003). Nearly all of our experimental studies produce strongly kinetically limited growth that cannot be reasonably explained with the capacitance theory.

Commonly used values for α in cirrus cloud modeling are presented in Table 3.3. Only the Demott et al. (1998), Lin (2002), and Murphy (2003) models used values in

Category	Deposition Coefficient (α)			Radius (μm)
	Predicted	Max	Min	
3035	0.0088	0.038	0.015	10.7
3040a	0.016	0.017	0.0094	11.7
3040a	0.017	0.016	0.009	10.4
3040a	0.034	0.023	0.018	7.6
3040a	0.07	0.13	0.06	5.8
3040a	0.065	0.16	0.08	8.6
3035	0.11	0.11	0.069	7.7
3035	0.12	0.13	0.062	8.2
3040a	0.04	0.053	0.032	8.9
3040a	0.016	0.017	0.0091	9.9
3040b	0.014	0.011	0.006	12
3040b	0.06	0.057	0.031	6.3
3040b	0.022	0.02	0.012	9.6
3045	0.01	0.0095	0.0053	10.3
3045	0.013	0.02	0.011	9.2
3045	0.023	0.026	0.017	8.2
3045	0.012	0.013	0.0079	8.9

Table 3.2. Time-averaged deposition coefficients for the Scrit and supersaturation pair that minimizes the global minimum error for each of the 17 particle growths. The maximum and minimum error bounds are the time-averaged deposition coefficients for model fits based on saturation and initial radius errors.

Cirrus Model Deposition Coefficient Reference		
Jensen	1.0	Jensen et al. (1994)
Demott	0.04	Demott et al. (1998)
Cotton	0.24	Spice et al. (1999)
Kärcher	0.5	Lin et al. (2002)
Murphy	0.15	Murphy (2003)
Sassen	0.36	Sassen and Benson (2000)
Lin	0.1	Lin et al. (2002)

Table 3.3. Particle-averaged deposition coefficients used in recent cirrus cloud models.

their models near those predicted by this study or suggested by Magee (2006). Other models (e.g. Jensen et al., 1994; Lin et al., 2002) use values that are a factor of 2-10 larger than those predicted in this study and suggested by Magee (2006). It is important to note that values used in models are not necessarily based on laboratory data, and are provided here for reference. While conditions in cirrus clouds may vary widely and include growth warmer than -30 °C, α values used in cirrus modeling demonstrate that further work to better characterize α values is needed. More accurate values for α in models are also important because the deposition coefficient is a major component in determining the ice number concentration in cirrus clouds (Lin et al., 2002).

Particle growth runs that resulted in the cases with the largest α also had the lowest S_{crit} values (< 0.62%) and that are also lower than the S_{crit} values derived from Libbrecht's (2003) data (Zhang and Harrington, 2013). In all but one case, results with the highest α occurred where the relative error (see above) was minimized at lower supersaturation than the mean measured value. Additionally, if the low saturation (3035) cases are excluded, four of the five highest deposition coefficients correspond to particle growths where error-minimized saturations fall below measured values. Growths were simulated within measured supersaturation ranges, and the critical supersaturation

increased and the average α decreased. When this occurs, α_c and α_a (the axis-dependent deposition coefficients) differ by an order of magnitude (i.e. α_c=0.0035 and α_a=0.036), thereby implying a strong columnar habit generation would be necessary to produce growth matching laboratory data. This α difference between the axes is two to four times larger than for particles where results are within measured supersaturation ranges, and suggests a more extreme column habit would be necessary to reproduce laboratory data.

There is also a clear and intriguing trend between α and initial particle size. Seven of the eight smallest particles (including the five smallest) produced the seven largest deposition coefficients derived in the KLAH model (see Table 3.2). Additionally, a physical manifestation of this trend can be seen in Figure 3.11 where these smaller particles generally grow faster than their larger counterparts at the same saturation state. As a result, there is physical evidence in the laboratory data that smaller particles tend to grow more quickly relative to larger particles, as suggested in the work of Sheridan et al. (2009). Moreover, these results suggest there may be a correlation between size and α for small particles beyond the local supersaturation effect of small particles discussed by Sheridan (2008) who showed that small particles generally have larger α values because the local supersaturation is greater. However, Sheridan et al. (2009) also showed that initially smaller particles can grow to greater masses than initially larger particles in the same time. The results here suggest that these two mechanisms may be coupled; however, further particle growth studies are necessary to confirm the presence of such a correlation.

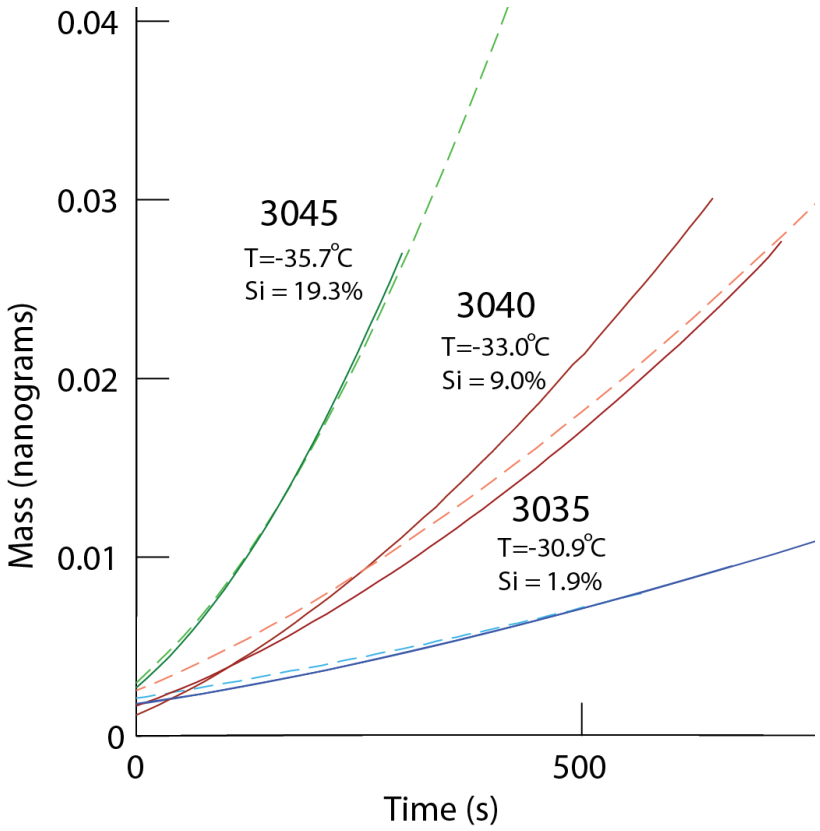

Figure 3.11. Mass growth curves with higher α values (solid traces) compared to other growths under the same conditions (dashed traces). All data points are included in this plot for clarity of each particle's growth trajectory. Some traces are truncated at the edge of the plot. See Figure 3.4 for error bounds information.

Finally, S_{crit} values were analyzed for correlations with temperature and supersaturation state (Figure 3.12). It appears as though S_{crit} may vary quazi-linearly with saturation state between -31 °C and -34°C, but increase more rapidly thereafter. For the higher temperature cases (> -34 °C), S_{crit} values derived are close to those derived from Libbrecht's (2003) data by Zhang and Harrington (2013). At the lowest temperatures (therefore highest supersaturation), S_{crit} appears to rise rapidly. These high S_{crit} values at the lowest temperature correspond to low α values (< 0.025). These results should not be considered conclusive until more data are collected at the lowest temperatures because only four growth runs at one chamber initialization were completed. Furthermore, the S_{crit}

values derived from Libbrecht (2003) fall within the maximum uncertainty error range for these growth runs (see Figure 3.12 shaded region). Errors in initial radius that lead to initial mass errors are larger at the lowest temperatures, and this contributes to the greater range of S_{crit}. Considering the large increase in supersaturation (a factor of two) compared to mid-saturation cases, the modest increase in growth speed (evident in the length of the growth record as well as the mass traces since relative mass is effectively capped by the instrument) suggests that the S_{crit} increase near -36 °C is plausible.

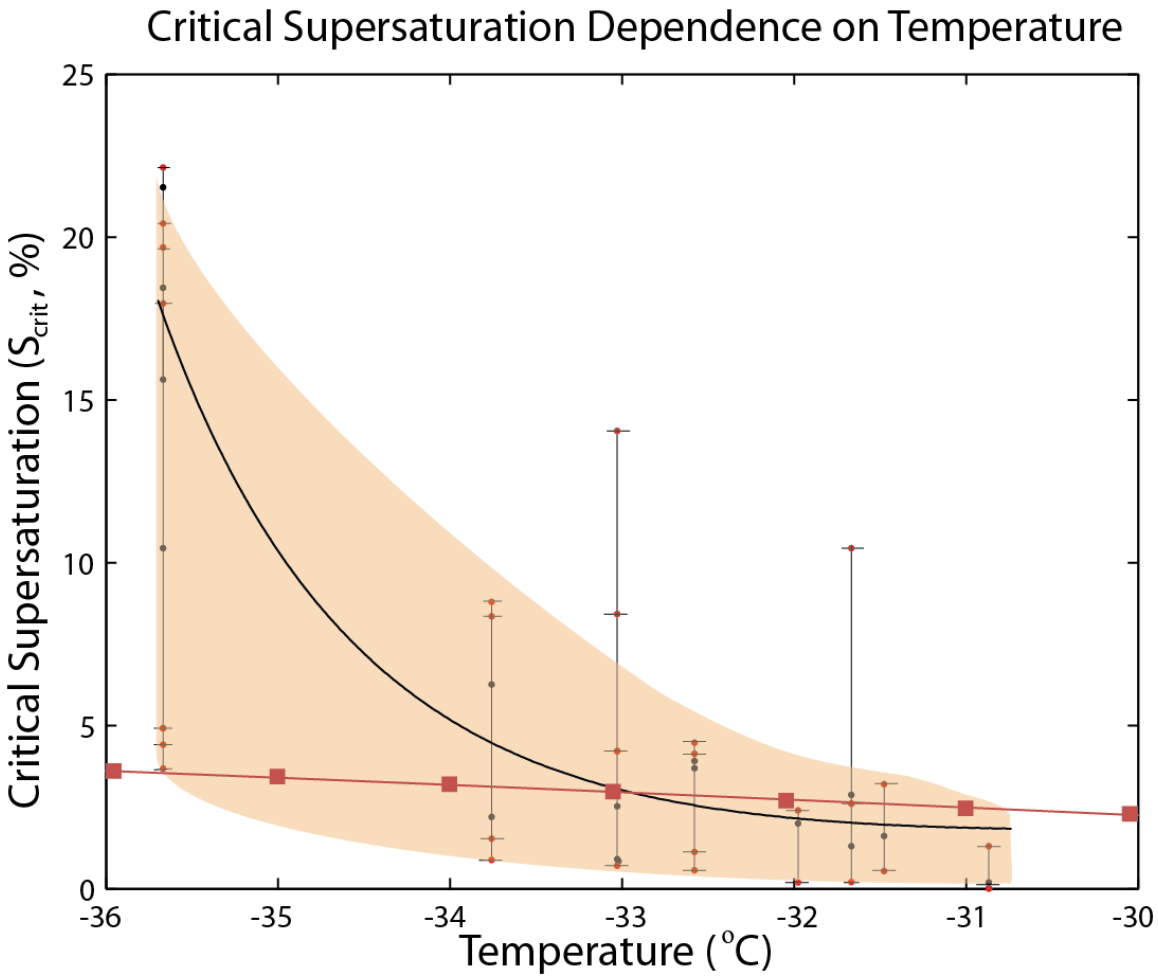

Figure 3.12. Critical supersaturation dependence on temperature, with best fit values denoted with a black line and plausible solutions based on measurement errors denoted with the shading. Black dots denote solutions where corresponding error ranges are plotted as red dots. Critical supersaturation derived from Libbrecht (2003) and from Zhang and Harrington (2013) is plotted in dark red squares.

Additional data over a wider range of temperatures and saturation states is necessary in order to come to a definitive interpretation of trends of critical supersaturation on temperature as well as to confirm the plausibility of a sharper increase in S_{crit} at temperatures below -35 °C. Trends observed in relation to saturation state and temperature are discernible, but the separation of temperature trends from saturation trends is not inherently possible at this time due to the limitations imposed on experimental conditions discussed earlier in this chapter. Increases in supersaturation in the chamber correspond to decreases in temperature because the top plate temperature of the BEL chamber is held constant.

Chapter 4

Discussion and Conclusion

In this study, the viability of the BEL diffusion chamber for ice crystal growth measurements was demonstrated. Small ice crystals (radii of 6-12 μm, typically 9-11 μm) were grown at temperatures between -30 °C and -37 °C at supersaturations over ice between 2% and 30%. The crystals were levitated in stable thermal and ice supersaturated conditions for up to one hour, and grown by vapor diffusion to between 10 and 40 times their initial mass. The maximum final size of the ice particle was dependent on initial charge on the particle, which is constant, and on the bottom plate voltage. The inclusion of automated particle tracking and recording allowed for more accurate positioning of growing particles than possible by manual means. Automated tracking was a breakthrough for accurate operation of the chamber and data collection, greatly reducing uncertainty and error, and is highly recommended for future devices. The tracking software was able to maintain the vertical location of the particle within 0.1 mm while recording data at up to 30 Hz. The BEL device produces growth data under relatively well-known conditions that is analyzed with the KLAH model.

The KLAH model (Zhang and Harrington, 2013) was vetted for its ability to capture the surface processes associated with growth at low temperatures and low saturation. Though the method compared well to a detailed solution for the growth of hexagonal crystals, it had not yet been used in conjunction with actual laboratory derived growth data. However, laboratory data that provides information on either the critical supersaturations or α are relatively scarce in the literature. Furthermore, rarely are

laboratory data used in conjunction with an ice crystal growth model developed specifically to utilize laboratory analyses as tools to improve the model. Utilizing BEL chamber data as inputs, the KLAH model is used to derive the critical supersaturations and deposition coefficients necessary to reproduce the laboratory data. Though the KLAH model is used for this purpose, the ability of the model to reproduce the magnitude and shape of the growth curves provides a way to test its performance. Traditionally, the deposition coefficient is given a constant value in many applications, even though it must change with temperature, supersaturation, and surface types. For instance, very rough ice surfaces have deposition coefficients of nearly unity, whereas smooth surfaces can have small values less than 0.01.

Results of comparisons among the laboratory data generally indicate that the KLAH model, by including surface kinetic processes, performs far better than the capacitance model, which generally overestimates the growth rates by an order of magnitude in many cases. Furthermore, the capacitance model is unable to reproduce the shapes of most of the laboratory growth curves, whereas the KLAH model is able to reproduce the curves with appropriate selection of critical supersaturations within measured saturation conditions inside the chamber. The work of Zhang and Harrington (2013) used critical supersaturations derived from the deposition coefficient data of Libbrecht (2003). At higher temperatures, there is less disagreement among the values of the critical supersaturation derived here from our laboratory data using the KLAH method, and the values derived from Libbrecht (2003). However, at low temperatures, there is a distinct increase in the derived S_{crit} value necessary to reproduce mass traces from the BEL chamber. The values derived from Libbrecht (2003) do show an increase in

S_{crit} with decreasing temperature (from 3% to 6% over a temperature range of -31 °C to -36 °C); however, analysis of BEL chamber data suggests far higher S_{crit} values (4% to 15%) over the same range of temperature.

Because the KLAH model predicts α with only critical saturation as an unknown parameter, values of α can be derived from the BEL chamber data. The deposition coefficients vary with supersaturation, but because the supersaturation is constant in the chamber the deposition coefficient remains roughly constant in time after the particle becomes sufficiently large. Variations in α exist initially when the particles are small, and this is reasonable given that growth kinetics are stronger when the size of the particles on the order of the mean free path of water molecules. However, this variation is critical as it allows the shape of the growth curve to vary in time, something that is not possible with a constant deposition coefficient. This variability allows for a better fit with the data than if the deposition coefficient is constant, and emphasizes the point made by Magee et al. (2006) that a single value of the deposition coefficient is not sufficient to fit laboratory-derived growth data. The values of α derived from laboratory data suggest that averaged values do not exceed 0.09 and can be as small as 0.003 (similar to Magee et al., 2006). Deposition coefficients are predicted to be relatively high (above 0.1) for two of the particles that were grown in one set of conditions with relatively high temperatures and low supersaturations (T = -30.85 °C, S_i < 2%). These derived values for α are all for temperatures below -30 °C, conditions for which α is rarely explored. The values derived from BEL chamber data in this study suggest that α routinely falls between 0.01 and 0.1 for small particles at low temperatures. The values that are derived here are similar to those derived from other studies (e.g. Libbrecht,2003; Gierens et al., 2003) and the lowest

deposition coefficients fall in line with α values suggested by Magee (2006); however, the largest values derived from our data also compare to those from other experiments (Strotzki et al., 2013). Consequently, our results indicate that if the deposition coefficient is predicted, rather than assumed constant, the entire range of previously derived deposition coefficients can be reproduced. This is a distinct advantage of the KLAH method approach. At present, reasons for the variability in the critical supersaturations and deposition coefficients derived here remain somewhat obscure and future work will need to be done to understand the physical reasons for that variability.

The BEL chamber works well to grow crystals; however it does have its limitations. The initial size of the particle is determined with Mie scattering diffraction fringes immediately after launch. The determination of the initial particle sizes is currently the biggest limitation of the chamber because it influences both the determination of the initial particle mass as well as the measurement of the ice supersaturation with sulfuric acid drops (hence the relatively large range of possible supersaturations indicated in Chapter 3 above). Due to the requirement of removing the launcher, there is a small lag time between sizing the particle and determining the initial voltage, and this produces a systematic error in the mass measurement of the particle throughout its entire growth due to normalized voltage-based measurements. Another limitation of the BEL instrument is the inability to determine the habit of the particle grown. While not observed directly, it was evident that the particle possesses facets (i.e. Figure 3.1); however, whether they are polycrystalline or simple hexagonal facets is not known. Additional challenges faced with the BEL chamber were associated with the

launching and observing of particles. Details on these challenges can be found in Appendix B.

Despite the limitations, the BEL chamber and the KLAH model combination is able to provide useful information on the growth of ice particles at low temperatures and ice supersaturations. The errors in the laboratory data naturally influence the information derived from the KLAH model, and therefore the results are limited by errors in the initial particle size and saturation state. While results obtained from this study shed light on small crystal growth at low temperatures, more data are needed to arrive at more definitive conclusions. For future work, additional growth runs need to be conducted at lower temperatures and supersaturations as this would significantly improve upon the robustness of this study. Also, a method for viewing the crystal structure of the particles growing in the chamber (e.g. capturing crystals and transferring them to an electron microscope) is highly desired. There is some ancillary evidence of the habit forms grown in the chamber in that a column-like structure has been observed on the bottom plate of the BEL chamber after crystal growth runs occurred, but it is impossible to state with certainty if it was the levitated particle. Lastly, additional work on the saturation state inside the BEL chamber (Chapter 2) is needed to improve the robustness of the aforementioned results. This is the single most important measurement that needs to be improved. Until the supersaturation inside the chamber is better known, the span of S_{crit} and α values determined in this study will remain relatively large. However, it is important to keep in mind that determining the saturation state inside a chamber is difficult, which is likely the reason that some studies use the minimization of an ice growth model as a way to determine the saturation state (e.g. Swanson et al., 1999).

Growth data from the BEL diffusion chamber analyzed with the KLAH single crystal model strongly indicates the importance of surface molecular processes (kinetic resistance) for ice growth models. It is evident that improving our understanding of kinetically limited growth in terms of α is important for future work on ice growth modeling.

REFERENCES

Bacon, N. J., M. B. Baker, and B. D. Swanson, 2003: Initial stages in the morphological evolution of vapour-grown ice crystals: A laboratory investigation. *Q.J.R.Meteorol.Soc.*, **129**, 1903-1927, doi:10.1256/qj.02.04.

Bailey, M., J. Hallett, 2002: Nucleation effects on the habit of vapour grown ice crystals from -18 to -42°C. *Q.J.R.Meteorol.Soc.*, **128**, 1461-1483, doi:10.1002/qj.200212858304.

Bailey, M., J. Hallett, 2004: Growth Rates and Habits of Ice Crystals between -20° and -70°C. *J.Atmos.Sci.*, **61**, 514-544.

Bailey, M. P., J. Hallett, 2009: A Comprehensive Habit Diagram for Atmospheric Ice Crystals: Confirmation from the Laboratory, AIRS II, and Other Field Studies. *J.Atmos.Sci.*, **66**, 2888-2899, doi:10.1175/2009JAS2883.1.

Bartlett, J.T., A.P. Van Den Heuval, B.J. Mason, 1963: The growth of ice crystals in an electric field, *Z. Angew. Math. Phys*., **14**, 599–610.

Burton, W. K., N. Cabrera, and F. C. Frank, 1951: The Growth of Crystals and the Equilibrium Structure of their Surfaces. *Philosophical Transactions of the Royal Society of London.Series A, Mathematical and Physical Sciences*, **243**, 299-358, doi:10.1098/rsta.1951.0006.

Carslaw, K. S., S. L. Clegg, and P. Brimblecombe, 1995: A thermodynamic model of the system. HCl - HNO3 - H2SO4 - H2O, including solubilities of HBr, from <200 to 328 K. - *J. Phys. Chem.*, **99**, 11557-11574, doi:- 10.1021/j100029a039.

Chen, J., D. Lamb, 1994: The Theoretical Basis for the Parameterization of Ice Crystal Habits: Growth by Vapor Deposition. *J.Atmos.Sci.*, **51**, 1206-1222, doi:10.1175/1520-0469(1994)051

Chiruta, M., P. K. Wang, 2005: The capacitance of solid and hollow hexagonal ice columns. *Geophys.Res.Lett.*, **32**, - L05803, doi:10.1029/2004GL021771.

COTTON, W. R., 1972: Numerical Simulation of Precipitation Development in Supercooled Cumuli - Part I. *Mon.Wea.Rev.*, **100**, 757-763, doi:10.1175/1520-0493(1972)100

Crowther, A., 1973: Preliminary investigation into the growth of ice crystals from the vapour in an electric field in the temperature range -11 to -15 °C. *J. of Crys. Gr*., **13-14**, 241-243.

Davis, E. J., 1997: A History of Single Aerosol Particle Levitation. *Aerosol Science and Technology*, **26**, 212-254, doi:10.1080/02786829708965426.

Davis, E. A., 2010: A button electrode levitation chamber for the study of ice crystal growth under atmospheric conditions. M.S. thesis, Dept. of Meteorology, The Pennsylvania State University, 77 pp.

DeMott, P. J., M. P. Meyers, and W. R. Cotton, 1994: Parameterization and Impact of Ice initiation Processes Relevant to Numerical Model Simulations of Cirrus Clouds. *J.Atmos.Sci.*, **51**, 77-90, doi:10.1175/1520-0469(1994)051.

Demott, P.J., D. C. Rogers, S. M. Kreidenweis, Y. Chen, C. H. Twohy, D. Baumgardner, A. J. Heymsfield, and K. R. Chan, 1998: The role of heterogeneous freezing nucleation in upper tropospheric clouds: Inferences from SUCCESS. *Geophys. Res. Lett.*, 25, 1387–1390.

Flatau, P. J., R. L. Walko, and W. R. Cotton, 1992: Polynomial Fits to Saturation Vapor Pressure. *J.Appl.Meteor.*, **31**, 1507-1513, doi:10.1175/1520-0450(1992)031.

Fletcher, N. H., 1973: Dendritic growth of ice crystals. *J.Cryst.Growth*, **20**, 268-272, doi:10.1016/0022-0248(73)90090-0.Fukuta, Norihiko, Tsuneya Takahashi, 1999: The growth of atmospheric ice crystals: a summary of findings in vertical supercooled cloud tunnel studies. *J. Atmos. Sci.*, **56**, 1963–1979. doi: 10.1175/1520-0469(1999)056

Gierens, K. M., M. Monier, and J. Gayet, 2003: The deposition coefficient and its role for cirrus clouds. *Journal of Geophysical Research: Atmospheres*, **108**, - 4069, doi:10.1029/2001JD001558.

Goff, J. A., S. Gratch, 1946: Low-pressure properties of water from −160 to 212 °F. *Trans. ASHVE*, **52**, 95-121.

Harrington, J. Y., K. Sulia, and H. Morrison, 2013: A Method for Adaptive Habit Prediction in Bulk Microphysical Models. Part I: Theoretical Development. *J.Atmos.Sci.*, **70**, 349-364, doi:10.1175/JAS-D-12-040.1.

Harrington, J. Y., K. Sulia, and H. Morrison, 2013: A Method for Adaptive Habit Prediction in Bulk Microphysical Models. Part II: Parcel Model Corroboration. *J.Atmos.Sci.*, **70**, 365-376, doi:10.1175/JAS-D-12-0152.1.

Hashino, T., G. J. Tripoli, 2007: The Spectral Ice Habit Prediction System (SHIPS). Part I: Model Description and Simulation of the Vapor Deposition Process. *J.Atmos.Sci.*, **64**, 2210-2237, doi:10.1175/JAS3963.1.

Haynes, W. M., Ed., 2008: *CRC Handbook of Chemisty and Physics.* 89th ed. CRC Press.

Hu, D., B. Makin, 1991: Study of a five-electrode quadrupole levitation system; Theoretical aspects. *IEE Proceedings-A*, **138**, 320-336, doi:10.1049/ip-a-3.1991.0047.

Jensen, E. J., and O. B. Toon, Ice nucleation in the upper troposphere: Sensitivity to aerosol composition and size distribution, temperature, and cooling rate, *Geophys. Res. Lett.* ,21 , 2019–2022, 1994.

Kanji, Z. A., P. J. DeMott, O. Möhler, and J. P. D. Abbatt, 2011: Results from the University of Toronto continuous flow diffusion chamber at ICIS 2007: instrument intercomparison

and ice onsets for different aerosol types. *Atmos. Chem. Phys.*, **33-34**, doi:10.5194/acp-11-31-2011.

Keller, V. W., 1980: *Ice Crystal Growth in a Dynamic Diffusion Chamber*. NASA, 201 pp.

Kobayashi,T., 1960: *Phil. Mag*, 1363-1370.

Krieger, U. K., J. C. Mössinger, B. Luo, U. Weers, and T. Peter, 2000: Measurement of the Refractive Indices of H2SO4-HNO3-H2O Solutions to Stratospheric Temperatures. *Appl.Opt.*, **39**, 3691-3703.

Kuroda, T., R. Lacmann, 1982: Growth kinetics of ice from the vapour phase and its growth forms. *J.Cryst.Growth*, **56**, 189-205, doi:10.1016/0022-0248(82)90028-8.

Libbrecht, K. G., V. M. Tanusheva, 1998: Electrically Induced Morphological Instabilities in Free Dendrite Growth. *Phys.Rev.Lett.*, **81**, 176-179, doi:10.1103/PhysRevLett.81.176.

Libbrecht, K., 2003: Growth rates of the principal facets of ice between −10°C and −40°C. *J.Cryst.Growth*, **247**, 530-540, doi:10.1016/S0022-0248(02)01996-6.

Libbrecht, K.G.: A Critical Look at Ice Crystal Growth Data, K. G. Libbrecht, arXiv:cond-mat/0411662 (2004).

Libbrecht, K.G., 2005: The physics of snow crystals. *Rep. on Prog. in Phys.*, **68**, 855. Lamb, D. and W.D. Scott (1972). Linear growth rates of ice crystals grown from the vapor phase. *J. Cryst. Growth*, **12**, 21–31.

Lamb, D., and W.D. Scott, 1974: The Mechanism of Ice Crystal Growth and Habit Formation. *J. Atmos. Sci.*, **31**, 570-580.

Lamb, D., and J. Verlinde, 2011: *The Physics and Chemistry of Clouds*. Cambridge University Press, 584 pp.

Lin, R.F., D. Starr, P.J. DeMott, R. Cotton, K. Sassen, E. Jensen, B. Karcher, and X. Liu, 2002: Cirrus Parcel Model Comparison Project. Phase 1: The Critical Components to Simulate Cirrus Initiation Explicitly. *J. Atmos. Sci.,* **59**, No. 15, pp. 2305–2329.

Lohmann, U., P. Spichtinger, S. Jess, T. Peter, and H. Smit, 2008: Cirrus cloud formation and ice supersaturated region in a global climate model. *Environ. Res. Lett.*, **3,** 045022, doi10.1088/1748-9326/3/4/045022.

Magee, N. B., 2006: A laboratory investigation of vapor-grown ice crystals at low atmospheric temperatures, Ph.D. dissertation,The Pennsylvania State University, 249pp.

Magee, N., K. Spector, Y. Lin, C. Tong, and J. Beatty, 2011: Initial Ice Microparticle Sublimation Measurements from the Levitating Upper-Tropospheric Environmental

Simulator (LUTES). *J.Atmos.Oceanic Technol.*, **28**, 884-890, doi:10.1175/JTECH-D-11-00028.1.

Markov, I. V., 2003: *Crystal Growth for Beginners: Fundamentals of Nucleation, Crystal Growth, and Epitaxy.* Word Scientific, 564 pp.

Meyers, M. P., R. L. Walko, J. Y. Harrington, and W. R. Cotton, 1997: New RAMS cloud microphysics parameterization. Part II: The two-moment scheme. *Atmos.Res.,* **45**, 3-39.

Millikan, R.A., 1911: The Isolation of an ion, a precision measurement of its charge, and the correction of stokes's law, *Phys. Rev.*, **32**, 349-397.

Mitchell, D.L., 1994: A model predicting the evolution of ice particle size spectra and radiative properties of cirrus clouds, Part 1: Microphysics. *J. Atmos. Sci.*, **51,**797-816.

Morrison, H., W. W. Grabowski, 2008: Modeling Supersaturation and Subgrid-Scale Mixing with Two-Moment Bulk Warm Microphysics. *J.Atmos.Sci.,* **65**, 792-812, doi:10.1175/2007JAS2374.1.

Murphy D.M., 2003: Dehydration in cold clouds is enhanced by a transition from cubic to hexagonal ice. *Geophys. Res. Lett*., **30**, no. 23

Nakaya, U., 1954: *Snow Crystals: Natural and Artificial,* Harvard University Press, Cambridge, 510pp.

Nelson, J., 1994: A theoretical study of ice crystal growth in the atmosphere. Ph.D. dissertation, University of Washington, 183 pp.

Nelson, J. T., M. B. Baker, 1996: New theoretical framework for studies of vapor growth and sublimation of small ice crystals in the atmosphere. *J. Geophys. Res.: Atmos.*, **101**, 7033-7047, doi:10.1029/95JD03162.

Nelson, J., C. A. Knight, 1996: A new technique for growing crystals from the vapor. *J.Cryst.Growth*, **169**, 795-797, doi:10.1016/S0022-0248(96)00718-X.

Nelson, J., C. Knight, 1998: Snow Crystal Habit Changes Explained by Layer Nucleation. *J.Atmos.Sci.*, **55**, 1452-1465, doi:10.1175/1520-0469(1998)055

Peterson, H., M. Bailey, and J. Hallett, 2010: Ice particle growth under conditions of the upper troposphere. *Atmos.Res.*, **97**, 446-449, doi:10.1016/j.atmosres.2010.05.013.

Pflaum, J. C., H. R. Pruppacher, 1979: A Wind Tunnel Investigation of the Growth of Graupel Initiated from Frozen Drops. *J.Atmos.Sci.*, **36**, 680-689, doi:10.1175/1520-0469(1979)036

Pruppacher, H. R., J. D. Klett, 1997: *Microphysics of Clouds and Precipitation.* 2nd ed. Vol. 18, Kluwer Academic Publishers, 954 pp.

Rogers, D. C., 1988: Development of a continuous flow thermal gradient diffusion chamber for ice nucleation studies. *Atmos.Res.,* **22**, 149-181, doi:10.1016/0169-8095(88)90005-1.

Sassen K., and S. Benson, 2000: Ice nucleation in cirrus clouds: A model study of the homogenous and heterogeneous modes. *Geophys. Res. Lett*., **27**, 521-524.

Schiebener, P., J. Straub, J. M. H. L. Sengers, and J. S. Gallagher, 1990: Refractive index of water and steam as function of wavelength, temperature and density. *J.Phys.Chem.Ref.Data,* **19**, 677-717, doi:10.1063/1.555859.

Shaw, R. A., D. Lamb, and A. M. Moyle, 2000: An Electrodynamic Levitation System for Studying Individual Cloud Particles under Upper-Tropospheric Conditions. *J.Atmos.Oceanic Technol.,* **17**, 940-948, doi:10.1175/1520-0426(2000)017.

Sheridan, L., 2008: Deposition coefficient, habit, and ventilation influences on cirriform cloud properties. M.S. thesis, Dept. of Meteorology, The Pennsylvania State University, 102pp.

Sheridan, L. M., J. Y. Harrington, D. Lamb, and K. Sulia, 2009: Influence of ice crystal aspect ratio on the evolution of ice size spectra during vapor depositional growth. J. Atmos. Sci., 66, 3732–3743.

Skrotzki, J., P. Connolly, M. Schnaiter, H. Saathoff, O. Möhler, R. Wagner, M. Niemand, V. Ebert, and T. Leisner: The accomodations coefficient of water molecules on ice-cirrus cloud studies at the AIDA simulation chamber, *Atmos. Chem. And Phys*., **13**, 4451-4466, doi:10.5194/acp-13-4451-2013

Spice A., DW. Johnson, PRA. Brown, AG. Darlison, CPR. Saunders, 1999: Primary ice nucleation in orographic cirrus cloud: A numerical simulation of the microphysics, *Quart. J. Royal Met. Soc.,* 125, 1637-1667.

Sulia, K., and J. Harrington, 2011: Ice aspect ratio influences on mixed-phase clouds: Impacts on phase partitioning in parcel models. *J. Geophys. Res*., 116, D21309, doi:10.1029/2011JD016298.

Swanson, B. D., N. J. Bacon, E. J. Davis, and M. B. Baker, 1999: Electrodynamic trapping and manipulation of ice crystals. *Q.J.R.Meteorol.Soc.*, **125**, 1039-1058, doi:10.1002/qj.49712555514.

Thermo Scientific, cited 2013: NESLAB ULT Series Bath Circulators Product Specifications. [Available online at http://www.thermoscientific.de/eThermo/CMA/PDFs/Product/productPDF_25047.pdf]

von Blohn, N., K. Diehl, S. K. Mitra, and S. Borrmann, 2009: Riming of Graupel: Wind Tunnel Investigations of Collection Kernels and Growth Regimes. *J.Atmos.Sci.*, **66**, 2359-2366, doi:10.1175/2009JAS2969.1.

Walko, R. L., W. R. Cotton, M. P. Meyers, and J. Y. Harrington, 1995: New RAMS cloud microphysics parameterization part I: the single-moment scheme. *Atmos.Res.,* **38**, 29-62, doi:10.1016/0169-8095(94)00087-T.

Westbrook, C. D., A. J. Heymsfield, 2011: Ice Crystals Growing from Vapor in Supercooled Clouds between -2.5° and -22°C: Testing Current Parameterization Methods Using Laboratory Data. *J.Atmos.Sci.,* **68**, 2416-2429, doi:10.1175/JAS-D-11-017.1.

Westbrook, C. D., R. J. Hogan, and A. J. Illingworth, 2008: The Capacitance of Pristine Ice Crystals and Aggregate Snowflakes. *J.Atmos.Sci.,* **65**, 206-219, doi:10.1175/2007JAS2315.1.

Wood, S. E., M. B. Baker, and D. Calhoun, 2001: New model for the vapor growth of hexagonal ice crystals in the atmosphere. *Journal of Geophysical Research: Atmospheres,* **106**, 4845-4870, doi:10.1029/2000JD900338.

Woods, C. P., M. T. Stoelinga, and J. D. Locatelli, 2008: Size Spectra of Snow Particles Measured in Wintertime Precipitation in the Pacific Northwest. *J.Atmos.Sci.,* **65**, 189-205, doi:10.1175/2007JAS2243.1.

Xue, H., A. M. Moyle, N. Magee, J. Y. Harrington, and D. Lamb, 2005: Experimental studies of droplet evaporation kinetics: Validation of models for binary and ternary aqueous solutions. *J.Atmos.Sci.,* **62**, 4310-4326.

Zhang, C., and J. Y. Harrington, 2013: Including surface kinetic effects in simple models of ice vapor diffusion. *J. Atmos. Sci.,* in press.

Appendix A

Coefficients of the 6th Order Polynomial Fit

a_1=6.10952665
a_2=0.501948366
a_3=0.186288989E-01
a_4=0.403488906E-03
a_5=0.539797852E-05
a_6=0.420713632E-07
a_7=0.147271071E-09

Source: Flatau et al., (1991).

Appendix B

Extra Challenges

The accomplishments of the BEL diffusion chamber were the culmination of years of resolving minor issues that prevented particles from being grown experimentally. First, it was quickly realized that Delrin® plastic was not suitable as a material to serve as the particle launching tube due its dissolution in sulfuric acid solution (thereby allowing the escape of the Syltherm® coolant). PVC was used as a substitute for the launching opening to allow for sulfuric acid drop saturation experiments to continue.

The tracking software discussed in Chapter two was initially developed without a sensitivity setting that could be readily modified. For small particles that the chamber was initially tested with, this method was sufficient. As the particles became larger, erroneous detections of increased particle reflection from larger particles due to the high sensitivity required to capture particles at the onset of experiments became a major issue. As a result, particle sensitivity controls were included in the tracking software that allows the particle to be the sole detected centroid throughout each stage of its growth. An example of the need for sensitivity controls is Figure 3.1.

Another troublesome component of the chamber was the glass launching tips. Originally, these were crafted by a glassblower from fused silica tubes. The original technique has since been lost, and new launcher tips created by molding fused silica proved to be too fragile for use in the chamber (see Figure B.1). These tips would shatter energetically upon the freezing of the water inside the tips as a result of a weak point or

stress remnant in the glass. As an alternative, glass tubes (fused silica's melting point was too high for our capabilities) were shrunken around capillary tubes with a 30 μm opening. This method was suggested by Raymond Shaw through personal communication with Al Moyle and Jerry Harrington. These tips could be created in the lab with a known sized opening. Additionally, these tips were less prone to shattering as a result of freezing, however with sufficient exposure to very low temperatures shattering could not be consistently avoided. Therefore, the launcher tip was required to be removed, and before ice growth could begin to be measured due to the voltage applied to the launcher.

Figure B.1. This image demonstrates the challenges faced with the shattering of glass launcher tips as a result of stress caused by phase change expansion of freezing water. As a result, laboratory data are limited a top plate temperature of -30°C.

During the winter months, the laboratory reaped the benefits of the low dew points experienced in central Pennsylvania during the winter months. Ice accumulation

on the chamber was minimal and views into the chamber were unobstructed. As the spring and summer months arrived, ambient moisture in the laboratory increased, therefore greatly increasing the accumulation of ice on the chamber. Despite a consistent supply of dry air (dew point <-45°C), the ice growth quickly blocked both the tracking and Mie scattering fringe camera views into the chamber. The extent of ice accumulation under the insulation can be clearly seen in Figure B.2. In order to conduct experiments, a method to contain dry air around the chamber was sorely needed. The solution was to

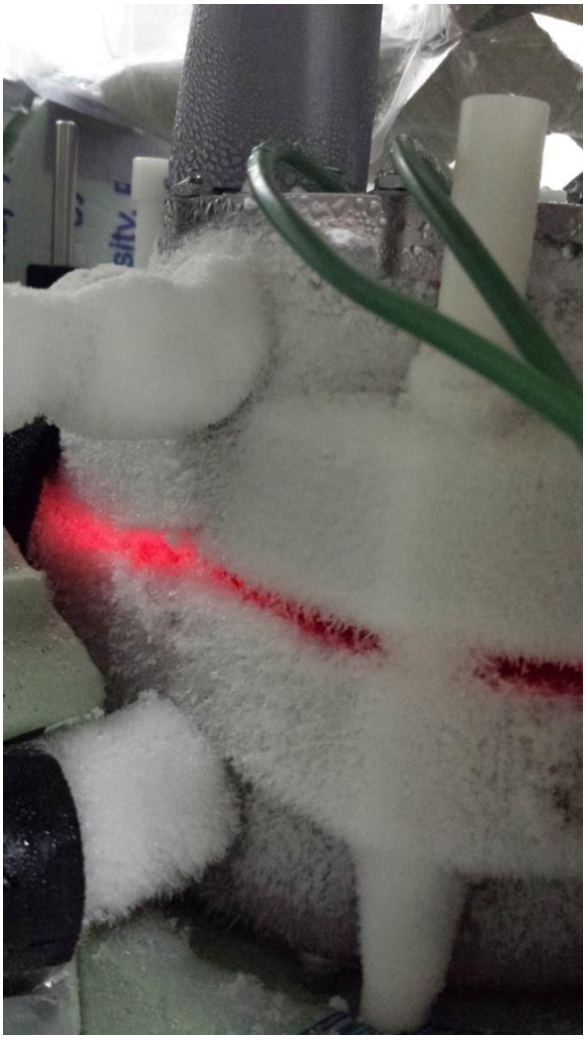

Figure B.2. Ice accumulation on the exterior surfaces of the BEL chamber without the implementation of a dry air containment system.

create a semi-air-tight plastic enclosure around the chamber. Dry air is supplied to the enclosure for half an hour before initialization of the experiment to ensure a dry environment on the exterior of the chamber. Future chambers will be designed with a Plexiglas® enclosure to ensure a dry environment around the chamber to prevent ice buildup from interfering with laboratory experiments.